Non-Hermitian linear electro-optic effect in three-dimensional materials

Tiago A. Morgado [1,*] Tatiana G. Rappoport [2,3] Stepan S. Tsirkin [4,5] Sylvain Lannebère [1]
Ivo Souza [4,5] and Mário G. Silveirinha [6,†]

[1]*Instituto de Telecomunicações and Department of Electrical Engineering, University of Coimbra, 3030-290 Coimbra, Portugal*
[2]*Centro de Física das Universidade do Minho e do Porto (CF-UM-UP) e Departamento de Física, Universidade do Minho, P-4710-057 Braga, Portugal*
[3]*Instituto de Física, Universidade Federal do Rio de Janeiro, C.P. 68528, 21941-972 Rio de Janeiro, RJ, Brazil*
[4]*Centro de Física de Materiales, Universidad del País Vasco, 20018 San Sebastián, Spain*
[5]*Ikerbasque Foundation, 48013 Bilbao, Spain*
[6]*University of Lisbon–Instituto Superior Técnico and Instituto de Telecomunicações, Avenida Rovisco Pais, 1,1049-001 Lisboa, Portugal*

Here, we present an in-depth theoretical analysis of the linear electro-optic effect in low-symmetry three-dimensional (3D) conductive materials with large Berry curvature dipoles. Our study identifies two distinct kinetic contributions to the linear electro-optic effect: a gyrotropic Hermitian (conservative) piece and a non-Hermitian term that can originate optical gain. We concentrate on the study of 3D materials belonging to the 32 (D_3) point group subject to a static electric bias along the trigonal axis. Our investigation shows that doped trigonal tellurium has promising properties, with its gyrotropic electro-optic response offering the potential for realizing electrically biased electromagnetic isolators and inducing significant optical dichroism. Most notably, it is demonstrated that under sufficiently large static electric bias, tellurium's non-Hermitian electro-optic response may lead to optical gain. Using first-principles calculations, it is shown that n-doped tellurium is particularly promising, as it can host significantly larger Berry curvature dipoles than the more common p-doped tellurium.

I. INTRODUCTION

Advances in integrated photonic circuits are key to meeting the demands of high-speed data communications, offering significant improvements in speed, bandwidth, and energy efficiency [1,2]. However, their development is challenged by the presence of losses and the difficulty of integrating non-reciprocal components [1,3–7]. These components, such as isolators and circulators, enable one-way light transmission, a crucial feature for efficient signal routing and control in photonic circuits.

The traditional and long-established approach to achieve robust nonreciprocal responses and realize electromagnetic isolators involves breaking time-reversal symmetry by exploiting magneto-optic effects in materials like ferrites or iron garnets under a static magnetic bias [8–10]. However, the requirement for an external bulky magnetic biasing circuit poses a major obstacle to integrating these components onto a chip. This issue has spurred the development of alternative "magnetless" nonreciprocal systems in recent years.

Magnetless nonreciprocal systems can be categorized into two distinct groups. The first group comprises systems with linear material responses under normal operating conditions, and which require the application of a suitable external

bias. This group includes various platforms characterized by broken time-reversal symmetry, such as time-variant systems [11–14], systems with moving parts [15,16], and systems with drifting electrons [17–22]. Furthermore, this category also encompasses proposals involving non-Hermitian platforms based on active electronic systems [23–25] or optically pumped systems [26]. The second group comprises nonreciprocal systems that rely on the use of nonlinear materials, which are dynamically self-biased by incoming waves [27–32]. The latter solutions require high-power input signals and usually do not offer robust optical isolation [33,34].

In recent years, there has been significant interest in nonlinear transport phenomena [35], particularly nonlinear Hall and linear electro-optic (EO) effects and their relationship with the Berry curvature dipole [36–38]. The Berry curvature dipole may be pictured as a dipolar pattern of the Berry curvature distribution across the Fermi surface.

Some time ago, inspired by the physics of transistors, we introduced a mechanism for generating strongly nonreciprocal and non-Hermitian linearized electromagnetic responses in low-symmetry materials [39]. Our approach relies on the combination of material nonlinearities with a static electric bias. We theoretically demonstrated that a hypothetical metamaterial, composed of a periodic arrangement of MOSFETs (termed "MOSFET-metamaterial") exhibits intriguing nonreciprocal and non-Hermitian responses with unique physical properties under a static electric bias.

Our theory raises the question of whether it is possible to achieve a distributed electromagnetic response akin

*Corresponding author: tiago.morgado@co.it.pt
†mario.silveirinha@tecnico.ulisboa.pt

to that of a transistor using natural materials. In a recent theoretical study [38], we have demonstrated that non-linear two-dimensional (2D) conductive materials with a broken inversion symmetry and a large Berry curvature dipole (e.g., strained twisted bilayer graphene) are promising platforms to obtain nonreciprocal and non-Hermitian transistorlike distributed responses. The analysis of Ref. [38] shows that an incident electromagnetic wave passing through such electrically biased 2D materials may experience optical gain, depending on the wave polarization, direction of wave propagation, and orientation of the static electric bias. An optical cavity comprising these electrically biased 2D non-Hermitian materials may enable chiral terahertz (THz) lasing [40].

In this paper, we extend our theory to three-dimensional (3D) crystals with broken inversion symmetry and a Berry curvature dipole. Consistent with our previous investigation on 2D low-symmetry materials [38], we find that there are two distinct contributions to the linear EO effect in these 3D materials: one is rooted in a gyrotropic Hermitian (conservative) response, and the other is associated with a non-Hermitian EO response characterized by its nonconservative nature. Moreover, we analyze the origin for the gyrotropic EO effect, suggesting that it arises from microscopic dc currents following helical-type trajectories induced by the static electric bias, which in turn generate an internal static magnetic field.

It is important to point out here the differences between the EO effect and the nonlinear Hall effect [36]. While both effects are linked to the Berry curvature dipole, they diverge in key aspects. Specifically, the EO effect manifests as a linear response to the combined influence of a static electric field bias ($\mathbf{E}_0$) and an optical dynamic (ac) electric field ($\mathbf{E}_\omega e^{-i\omega t}$). On the other hand, the nonlinear Hall effect is a second-order response to an applied electric field.

Throughout this work, we focus the study of the linear EO effects on 3D materials belonging to the 32 point group (D_3 in the Schoenflies notation) subject to a static electric bias along the trigonal axis. Using first-principles density functional theory (DFT) calculations, we provide an in-depth study of the linear EO effect in trigonal tellurium. It is demonstrated that the gyrotropic Hermitian response in *n*-doped tellurium may present exciting opportunities, e.g., the realization of electrically biased electromagnetic isolators and the generation of significant optical dichroism. Indeed, the first-principles calculations suggest that *n*-doped tellurium may provide larger Berry curvature dipoles and lower dc conductivity in comparison with the more common *p*-doped variant. Moreover, under a sufficiently high static electric bias, the non-Hermitian EO response of tellurium may give rise to optical gain.

This paper is organized as follows. In Sec. II, we derive the gyrotropic (Hermitian) and non-Hermitian linear EO responses of generic 3D low-symmetry conductive systems. In Sec. III, we examine the linear EO effect in generic 3D materials belonging to the 32 point group symmetry (D_3). Finally, in Sec. IV we investigate nonreciprocal and gain effects in trigonal tellurium biased along the trigonal axis. The conclusions are drawn in Sec. V.

II. NON-HERMITIAN LINEAR ELECTRO-OPTIC EFFECT IN LOW-SYMMETRY MATERIALS

A. Boltzmann transport theory

Here, we use the semiclassical Boltzmann transport theory to derive the linearized optical response of a generic low-symmetry metallic system under a static electric bias. We suppose that the material is described by a time-reversal symmetric Hamiltonian. Our analysis does not take into account self-consistent field (screening) effects.

The electron distribution function in the material, $f_{\mathbf{k}}$, satisfies the Boltzmann transport equation:

$$\frac{\partial f_{\mathbf{k}}}{\partial t} + \frac{\partial \mathbf{k}}{\partial t} \cdot \nabla_{\mathbf{k}} f_{\mathbf{k}} = -\frac{1}{\tau}(f_{\mathbf{k}} - f_{\mathbf{k}}^0), \tag{1}$$

where $f_{\mathbf{k}}^0$ is the Fermi-Dirac distribution, τ is the scattering relaxation time, and $\hbar \frac{\partial \mathbf{k}}{\partial t} = -e\mathbf{E}$ (with $e > 0$). For a static (dc) field $\mathbf{E}_0$ the distribution function does not depend on t. Thus, the perturbation due to the static bias is given by

$$\left[f_{\mathbf{k}} - f_{\mathbf{k}}^0\right]_{\text{static}} = \delta f_{\mathbf{k}}^0 \approx \frac{e}{\hbar}\tau \mathbf{E}_0 \cdot \nabla_{\mathbf{k}} f_{\mathbf{k}}^0. \tag{2}$$

Let us now suppose that a much weaker optical dynamic (ac) field ($\mathbf{E}_\omega e^{-i\omega t}$) is applied to the material, resulting in a perturbation ($\delta f_{\mathbf{k}}^\omega e^{-i\omega t}$) of the distribution function. The linearized dynamics of the optical field is controlled by the distribution function $f_{\mathbf{k}}^0 + \delta f_{\mathbf{k}}^0$, so that $\delta f_{\mathbf{k}}^\omega$ satisfies

$$\frac{\partial}{\partial t}\left(\delta f_{\mathbf{k}}^\omega e^{-i\omega t}\right) + (-e\mathbf{E}_\omega e^{-i\omega t})\frac{1}{\hbar} \cdot \nabla_{\mathbf{k}}\left[f_{\mathbf{k}}^0 + \delta f_{\mathbf{k}}^0\right]$$
$$= -\frac{1}{\tau}\delta f_{\mathbf{k}}^\omega e^{-i\omega t}. \tag{3}$$

Solving Eq. (3) with respect to $\delta f_{\mathbf{k}}^\omega$ it follows that

$$\delta f_{\mathbf{k}}^\omega = \frac{1}{1 - i\omega\tau}\frac{\tau e}{\hbar}\nabla_{\mathbf{k}}\left[f_{\mathbf{k}}^0 + \delta f_{\mathbf{k}}^0\right] \cdot \mathbf{E}_\omega$$
$$= \frac{1}{1-i\omega\tau}\frac{\tau e}{\hbar}\nabla_{\mathbf{k}} f_{\mathbf{k}}^0 \cdot \mathbf{E}_\omega + \frac{1}{1-i\omega\tau}\left(\frac{\tau e}{\hbar}\right)^2 \nabla_{\mathbf{k}}\left[\mathbf{E}_0 \cdot \nabla_{\mathbf{k}} f_{\mathbf{k}}^0\right] \cdot \mathbf{E}_\omega. \tag{4}$$

Next, we characterize the induced current density distribution due to the applied fields. It can be written in terms of the total distribution function as follows:

$$\mathbf{J} = -\frac{e}{V}\sum_{\mathbf{k}}\left(f_{\mathbf{k}}^0 + \delta f_{\mathbf{k}}^0 + \delta f_{\mathbf{k}}^\omega e^{-i\omega t} + \text{c.c.}\right)$$
$$\left(\mathbf{v}_{\mathbf{k}}^0 - \frac{e}{\hbar}\mathbf{\Omega}_{\mathbf{k}} \times (\mathbf{E}_0 + \mathbf{E}_\omega e^{-i\omega t} + \text{c.c.})\right), \tag{5}$$

where $\mathbf{v}_{\mathbf{k}}^0$ is the group velocity of the electron wave, $\mathbf{\Omega}_{\mathbf{k}}$ is the Berry curvature, V is the volume of the material, and c.c. stands for complex conjugate. Note that we take into account the anomalous velocity contribution, $-\frac{e}{\hbar}\mathbf{\Omega}_{\mathbf{k}} \times \mathbf{E}$ [41,42], which is the key mechanism to obtain both the non-Hermitian and the gyrotropic response. The anomalous velocity has higher-order corrections in the electromagnetic fields [43], but they have no impact in the EO response

of time-reversal symmetric systems. The linear response is determined by the following static and dynamic current densities:

$$\mathbf{J}^0 = -\frac{e}{V} \sum_{\mathbf{k}} \left(\mathbf{v}_{\mathbf{k}}^0 - \frac{e}{\hbar} \mathbf{\Omega}_{\mathbf{k}} \times \mathbf{E}_0 \right) \left(f_{\mathbf{k}}^0 + \delta f_{\mathbf{k}}^0 \right), \quad (6a)$$

$$\mathbf{J}^\omega = -\frac{e}{V} \sum_{\mathbf{k}} \left(\mathbf{v}_{\mathbf{k}}^0 - \frac{e}{\hbar} \mathbf{\Omega}_{\mathbf{k}} \times \mathbf{E}_0 \right) \delta f_{\mathbf{k}}^\omega$$
$$- \frac{e}{V} \sum_{\mathbf{k}} \left(-\frac{e}{\hbar} \mathbf{\Omega}_{\mathbf{k}} \times \mathbf{E}_\omega \right) \left(f_{\mathbf{k}}^0 + \delta f_{\mathbf{k}}^0 \right). \quad (6b)$$

As the system is described by a time-reversal symmetric Hamiltonian, $\mathbf{v}_{\mathbf{k}}^0$ and $\mathbf{\Omega}_{\mathbf{k}}$ are odd functions of the quasimomentum $\mathbf{k}$. Thus, only the terms associated with $\delta f_{\mathbf{k}}^0$ and $\delta f_{\mathbf{k}}^\omega$, which are also odd functions of $\mathbf{k}$, can contribute to the response:

$$\mathbf{J}_0 = -\frac{e}{V} \sum_{\mathbf{k}} \left(\mathbf{v}_{\mathbf{k}}^0 - \frac{e}{\hbar} \mathbf{\Omega}_{\mathbf{k}} \times \mathbf{E}_0 \right) \delta f_{\mathbf{k}}^0, \quad (7a)$$

$$\mathbf{J}_\omega = -\frac{e}{V} \sum_{\mathbf{k}} \left(\mathbf{v}_{\mathbf{k}}^0 - \frac{e}{\hbar} \mathbf{\Omega}_{\mathbf{k}} \times \mathbf{E}_0 \right) \delta f_{\mathbf{k}}^\omega$$
$$- \frac{e}{V} \sum_{\mathbf{k}} \left(-\frac{e}{\hbar} \mathbf{\Omega}_{\mathbf{k}} \times \mathbf{E}_\omega \right) \delta f_{\mathbf{k}}^0. \quad (7b)$$

Using now Eqs. (2) and (4), we can write the current as a function of the applied electric field:

$$\mathbf{J}_0 = -\frac{e}{V} \sum_{\mathbf{k}} \mathbf{v}_{\mathbf{k}}^0 \left(\frac{\tau e}{\hbar} \mathbf{E}_0 \cdot \nabla_{\mathbf{k}} f_{\mathbf{k}}^0 \right)$$
$$- \frac{e}{V} \sum_{\mathbf{k}} \left(-\frac{e}{\hbar} \mathbf{\Omega}_{\mathbf{k}} \times \mathbf{E}_0 \right) \left(\frac{\tau e}{\hbar} \mathbf{E}_0 \cdot \nabla_{\mathbf{k}} f_{\mathbf{k}}^0 \right) \quad (8a)$$

$$\mathbf{J}_\omega = -\frac{e}{V} \sum_{\mathbf{k}} \mathbf{v}_{\mathbf{k}}^0 \left(\frac{1}{1-i\omega\tau} \frac{\tau e}{\hbar} \nabla_{\mathbf{k}} f_{\mathbf{k}}^0 \cdot \mathbf{E}_\omega \right)$$
$$- \frac{e}{V} \sum_{\mathbf{k}} \left(-\frac{e}{\hbar} \mathbf{\Omega}_{\mathbf{k}} \times \mathbf{E}_0 \right) \left(\frac{1}{1-i\omega\tau} \frac{\tau e}{\hbar} \nabla_{\mathbf{k}} f_{\mathbf{k}}^0 \cdot \mathbf{E}_\omega \right)$$
$$- \frac{e}{V} \sum_{\mathbf{k}} \left(\frac{\tau e}{\hbar} \mathbf{E}_0 \cdot \nabla_{\mathbf{k}} f_{\mathbf{k}}^0 \right) \left(-\frac{e}{\hbar} \mathbf{\Omega}_{\mathbf{k}} \times \mathbf{E}_\omega \right). \quad (8b)$$

We only retain terms of $\mathbf{J}_\omega$ that are either independent of $\mathbf{E}_0$ or linear in $\mathbf{E}_0$. Higher-order terms are weaker and are not accounted for in our analysis. The leading terms in Eq. (8) associated with $\mathbf{v}_{\mathbf{k}}^0$ are the usual linear static and dynamic Drude-like responses. The linear EO response is ruled by the remaining terms:

$$\mathbf{J}_{\text{EO}} = \frac{\tau e^3}{\hbar^2} \mathbf{E}_0 \cdot \left(\frac{1}{V} \sum_{\mathbf{k}} \nabla_{\mathbf{k}} f_{\mathbf{k}}^0 \otimes \mathbf{\Omega}_{\mathbf{k}} \right) \times \mathbf{E}_\omega$$
$$+ \frac{\tau e^3}{\hbar^2} \frac{1}{1-i\omega\tau} \left(\frac{1}{V} \sum_{\mathbf{k}} (\mathbf{\Omega}_{\mathbf{k}} \times \mathbf{E}_0) \otimes \nabla_{\mathbf{k}} f_{\mathbf{k}}^0 \right) \cdot \mathbf{E}_\omega, \quad (9)$$

where the symbol $\otimes$ denotes the tensor product of two vectors. The EO current density ($\mathbf{J}_{\text{EO}}$) is ruled by the anomalous electron velocity. Specifically, it arises from the linear variation of the distribution function under the influence of one of the applied fields ($\mathbf{E}_0$ or $\mathbf{E}_\omega$), in conjunction with the anomalous velocity determined by the interplay between the Berry curvature and the other applied field ($\mathbf{E}_\omega$ or $\mathbf{E}_0$).

B. Conductivity response

The linear electro-optic response is determined by Eq. (9). The corresponding conductivity tensor can be written as a Brillouin-zone integral using the rule $\frac{1}{V} \sum_{\mathbf{k}} \to \frac{1}{(2\pi)^3} \int d^3\mathbf{k}$. Thus, the linear EO piece of the conductivity can be written as

$$\bar{\sigma}_{\text{EO}}(\omega) = \frac{\tau e^3}{\hbar^2} \left(\mathbf{E}_0 \cdot \frac{1}{(2\pi)^3} \int d^3\mathbf{k} \, \nabla_{\mathbf{k}} f_{\mathbf{k}}^0 \otimes \mathbf{\Omega}_{\mathbf{k}} \right) \times \bar{\mathbf{1}}$$
$$- \frac{\tau e^3}{\hbar^2} \frac{1}{1-i\omega\tau} \mathbf{E}_0 \times \left(\frac{1}{(2\pi)^3} \int d^3\mathbf{k} \, \mathbf{\Omega}_{\mathbf{k}} \otimes \nabla_{\mathbf{k}} f_{\mathbf{k}}^0 \right), \quad (10)$$

with $\bar{\mathbf{1}}$ the unit matrix. The conductivity can be expressed in terms of the so-called Berry curvature dipole tensor ($\bar{\mathbf{D}}$) defined as

$$D_{ij} = -\frac{1}{(2\pi)^3} \int \frac{\partial f_{\mathbf{k}}^0}{\partial k_i} \Omega_{\mathbf{k},j} d^3\mathbf{k} = \frac{1}{(2\pi)^3} \int f_{\mathbf{k}}^0 \frac{\partial \Omega_{\mathbf{k},j}}{\partial k_i} d^3\mathbf{k}. \quad (11)$$

The Berry curvature dipole in 3D materials is dimensionless and traceless: $D_{xx} + D_{yy} + D_{zz} = 0$. The conductivity $\bar{\sigma}_{\text{EO}}$ is given by

$$\bar{\sigma}_{\text{EO}}(\omega) = \bar{\sigma}_{\text{EO}}^{\text{H}} + \bar{\sigma}_{\text{EO}}^{\text{NH}}(\omega)$$
$$\equiv \frac{-\tau e^3}{\hbar^2} (\mathbf{E}_0 \cdot \bar{\mathbf{D}}) \times \bar{\mathbf{1}} + \frac{\tau e^3}{\hbar^2} \frac{1}{1-i\omega\tau} (\mathbf{E}_0 \times \bar{\mathbf{D}}^T), \quad (12)$$

where the symbol T denotes the tensor transpose.

The first term of $\bar{\sigma}_{\text{EO}}$ defines an antisymmetric real-valued matrix, analogous to a Hall conductivity. It corresponds to a conservative gyrotropic response associated with a pseudovector aligned along the direction of the vector $\mathbf{E}_0 \cdot \bar{\mathbf{D}} = \bar{\mathbf{D}}^T \cdot \mathbf{E}_0$ (pseudomagnetic field). This gyrotropic conservative response, which has been previously discussed in the literature [44], plays a crucial role in multiple phenomena, including the kinetic Faraday effect (also known as current-induced optical activity) [44–47] and the kinetic magnetoelectric effect [44,48,49]. Remarkably, $\bar{\sigma}_{\text{EO}}$ has an additional contribution ($\bar{\sigma}_{\text{EO}}^{\text{NH}}$) that varies with frequency and generally leads to a nonconservative electro-optic response and optical gain. This non-Hermitian electro-optic response was discovered only recently [38,50]. It should be noted that the derived EO response [Eq. (12)] is only valid for frequencies well below the threshold for interband absorption.

C. The Berry curvature dipole as a magnetoelectric coupling tensor

To provide some intuition on the origin of the electro-optic effect and on the physical interpretation of the Berry curvature dipole from an optics perspective, next we present a comparison between the linear EO response of (chiral) conductors and the response of magnetized (gyrotropic) materials.

To this end, let us start by analyzing the response of an electron gas biased with a static magnetic field [Fig. 1(a)]. A magnetized electron gas exhibits a gyrotropic response, which can be modeled by a conductivity tensor of the form
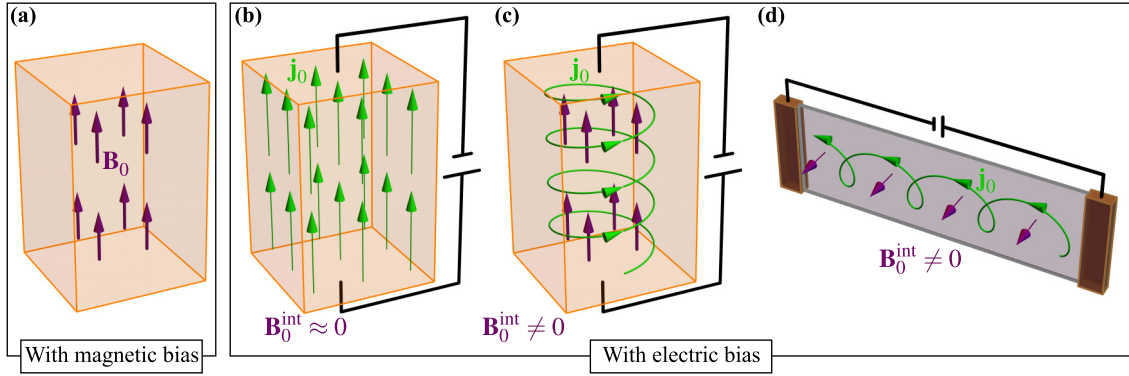
FIG. 1. (a) Electron gas biased by a static magnetic field ($\mathbf{B}_0$). The bias induces a gyrotropic electromagnetic response. (b) Semiconductor with mirror symmetry biased with a static electric field ($\mathbf{E}_0$): the average magnetic field in the bulk region is approximately zero, resulting in a negligible gyrotropic response. (c) Chiral low-symmetry semiconductor biased with a static electric field ($\mathbf{E}_0$). Due to the low symmetry of the material, the electric current $\mathbf{j}_0$ may follow a helical-type path, which creates an internal magnetic field and a gyrotropic electromagnetic response. (d) Similar to (c) but for a 2D system. In this case, the current trajectory has the form of a planar helix.

$\bar{\sigma}_{\text{gyro}} \approx \varepsilon_0 \frac{\omega_{\text{p}}^2}{\Gamma^2} \boldsymbol{\omega}_{\text{c}} \times \bar{\mathbf{1}}$, with ε_0 the vacuum permittivity, ω_{p} the plasma frequency, $\boldsymbol{\omega}_{\text{c}} = e\mathbf{B}_0/m^*$ the cyclotron frequency with m^* the effective mass of the electrons, and $\Gamma = 1/\tau$ the collision frequency associated with material loss. For simplicity, we focus on the low-frequency response of the material ($\omega \ll \Gamma$) and suppose that $|\omega_{\text{c}}| \ll \Gamma$.

It is interesting to compare the response of the magnetically biased electron gas with the first piece of Eq. (12). By matching $\bar{\sigma}_{\text{gyro}} \approx \varepsilon_0 \frac{\omega_{\text{p}}^2}{\Gamma^2} \boldsymbol{\omega}_{\text{c}} \times \bar{\mathbf{1}}$ to $\bar{\sigma}_{\text{EO}}^{\text{H}} = -\frac{\tau e^3}{\hbar^2}(\mathbf{E}_0 \cdot \bar{\mathbf{D}}) \times \bar{\mathbf{1}}$ one sees that the static electric bias induces an equivalent cyclotron frequency given by $\boldsymbol{\omega}_{\text{c}} = \frac{-e^3 \Gamma}{\varepsilon_0 \hbar^2 \omega_{\text{p}}^2}(\bar{\mathbf{D}}^T \cdot \mathbf{E}_0)$. Thus, the equivalent magnetic bias is given by

$$\mathbf{B}_0^{\text{int}} = \frac{-e^2 \Gamma m^*}{\varepsilon_0 \hbar^2 \omega_{\text{p}}^2} \bar{\mathbf{D}}^T \cdot \mathbf{E}_0 = -\frac{1}{c} \bar{\zeta} \cdot \mathbf{E}_0, \tag{13}$$

where $\bar{\zeta} = 4\pi \alpha_e \frac{m^* c^2}{\hbar \omega_{\text{p}}} \frac{\Gamma}{\omega_{\text{p}}} \bar{\mathbf{D}}^T$ is a dimensionless tensor, with $\alpha_e = \frac{e^2}{4\pi \varepsilon_0 \hbar c} \approx \frac{1}{137}$ the fine-structure constant. As seen, the Berry curvature dipole links the equivalent magnetic field to the static electric bias. Thus, $\bar{\mathbf{D}}^T$ may be understood as a static magnetoelectric coupling tensor. A related interpretation was presented in Ref. [51]. To give an idea of the numbers, suppose that $\Gamma/\omega_{\text{p}} \sim 1$, $m^* = 0.1 m_e$ with m_e the rest free-electron mass, $\omega_{\text{p}} \sim 2\pi \times 1$ THz, and $\bar{\mathbf{D}}^T \sim 10^{-4}$. Then, the electric field intensity required in order that $\mathbf{B}_0^{\text{int}} \sim 1$ mT is 2.6×10^3 V/m. The equivalent magnetic field intensity scales with the Berry curvature dipole, and hence materials with a large Berry curvature dipole can be promising platforms to generate strong nonreciprocal and non-Hermitian effects.

The previous discussion leads to an interesting picture for the physical origin of the (conservative part) of the linear EO effect. In fact, it suggests that in low-symmetry materials the static electric bias may create an internal static magnetic field that acts to bias the material. The effect may be pictured as a result of helical-type trajectories for the dc current, due to the low symmetry of the material [compare Figs. 1(b) and 1(c)]. In contrast, for materials with mirror symmetry the current trajectory follows a straight line, and thereby the induced magnetic field is mostly outside of the material and

the net magnetization within the material is approximately zero [Fig. 1(b)]. Consequently, the gyrotropic response is negligible in the high-symmetry case ($\bar{\sigma}_{\text{gyro}} \approx 0$). A related picture for the current trajectory in the material has been discussed elsewhere [52–54]. The same mechanism justifies the gyrotropic response of low-symmetry 2D materials biased with a static electric bias (see Ref. [38]). In this case, the microscopic currents may flow along planar helical paths, leading to a magnetic field orthogonal to $\mathbf{E}_0$ [see Fig. 1(d)].

Importantly, the current-induced gyrotropic effect has been experimentally observed in Refs. [45,46], by measuring the rotation of light polarization when passing through a biased tellurium sample. This electrical analog of the Faraday effect [55] was designated as current-induced optical activity [45,46] or kinetic Faraday effect [44].

III. MATERIALS WITH D_3 SYMMETRY

A. Electro-optic conductivity

Here we analyze the electro-optic effects in 3D materials belonging to the 32 point group. For such materials, the Berry curvature dipole tensor has the form [44]

$$\bar{\mathbf{D}} = D\hat{\mathbf{x}} \otimes \hat{\mathbf{x}} + D\hat{\mathbf{y}} \otimes \hat{\mathbf{y}} - 2D\hat{\mathbf{z}} \otimes \hat{\mathbf{z}}. \tag{14}$$

For a static electric field bias $\mathbf{E}_0 = E_0 \hat{\mathbf{z}}$ applied along the trigonal axis, the Hermitian (H) and non-Hermitian (NH) EO conductivity contributions are given by

$$\bar{\sigma}_{\text{EO}}^{\text{H}} = \frac{\tau e^3}{\hbar^2} 2DE_0 \hat{\mathbf{z}} \times \bar{\mathbf{1}}, \tag{15a}$$

$$\bar{\sigma}_{\text{EO}}^{\text{NH}}(\omega) = \frac{\tau e^3}{\hbar^2} \frac{DE_0}{1 - i\omega\tau} \hat{\mathbf{z}} \times \bar{\mathbf{1}}. \tag{15b}$$

Curiously, with D_3 symmetry, both conservative and non-conservative components exhibit identical structures: they are represented by an antisymmetric tensor. As further discussed below, the response described by $\bar{\sigma}_{\text{EO}}^{\text{NH}}(\omega)$ is inherently non-conservative.

For convenience we introduce an equivalent cyclotron-type frequency defined as

$$\omega_0 = \frac{\tau e^3}{\varepsilon_0 \hbar^2} D E_0 = 4\pi \alpha_e \frac{ec}{\hbar \Gamma} D E_0. \tag{16}$$

The frequency ω_0 is proportional to the dipole strength and to the electric field strength, and inversely proportional to the collision frequency ($\Gamma = 1/\tau$). The linear electro-optic conductivity can be written in terms of ω_0 as follows:

$$\bar{\sigma}_{EO}^H = 2\varepsilon_0 \omega_0 \hat{\mathbf{z}} \times \bar{\mathbf{1}}, \tag{17}$$

$$\bar{\sigma}_{EO}^{NH}(\omega) = \frac{\varepsilon_0 \omega_0}{1 - i\omega\tau} \hat{\mathbf{z}} \times \bar{\mathbf{1}}.$$

It is interesting to analyze the EO contribution to the power (per unit of volume) transferred from the optical field to the material (dissipated power). It is given by

$$p_{dis,EO} = \frac{1}{2} \mathrm{Re}\{\mathbf{E}^* \cdot \bar{\sigma}_{EO} \cdot \mathbf{E}\} = -\varepsilon_0 \omega_0 \frac{\omega\Gamma}{\omega^2 + \Gamma^2} \mathrm{Im}\{E_x E_y^*\}. \tag{18}$$

The transferred power is determined only by the nonconservative piece ($\bar{\sigma}_{EO}^{NH}$) of the EO conductivity. For simplicity, we dropped the subscript ω, and from here on the dynamic electric field is simply denoted by $\mathbf{E}$. Clearly, the sign of $p_{dis,EO}$ can be either positive, indicating absorption, or negative, indicating gain. The structure of $\bar{\sigma}_{EO}^{NH}$ shows considerable similarity to the response of a passive dissipative gyrotropic medium. However, here we can have gain because the linear EO effect does not trigger a corresponding "partner" diagonal (symmetric) response. This contrasts with passive systems, where the symmetric component of the response invariably ensures a positive value for $p_{dis,EO}$. For circular or elliptical polarization, the sign of the term $\mathrm{Im}\{E_x E_y^*\}$ is governed by the polarization handedness. Therefore, owing to the NH electro-optic contribution, power can be transferred either from the wave to the material (resulting in absorption, $p_{dis,EO} > 0$), or from the material to the wave (yielding optical gain, $p_{dis,EO} < 0$). It is relevant to note that $p_{dis,EO}$ is combined with an additional term $p_{dis,D} > 0$ due to the linear Drude response. This second term always generates dissipation.

A related discussion on power transfer in chiral metallic systems under the simultaneous influence of static (dc) and dynamic (ac) electric fields is reported in [50]. In addition, a study of the application of the nonlinear Hall effect to energy harvesting is presented in [56].

B. Full optical response

The full electromagnetic response of the material can be characterized by a permittivity tensor $\bar{\varepsilon}(\omega) = \bar{\varepsilon}_b + i\bar{\sigma}/\omega$, with $\bar{\sigma}(\omega) = \bar{\sigma}_D(\omega) + \bar{\sigma}_{EO}^H + \bar{\sigma}_{EO}^{NH}(\omega)$ describing the response of free electrons, and $\bar{\varepsilon}_b$ describing the permittivity response of bound electrons. Here $\bar{\sigma}_D(\omega)$ is the usual linear Drude response:

$$\bar{\sigma}_D(\omega) = \frac{\varepsilon_0 \omega_p^2}{\Gamma - i\omega} \bar{\mathbf{1}}. \tag{19}$$

For simplicity, we ignore here the typical anisotropic response of materials with D_3 symmetry, and we take $\bar{\varepsilon}_b$ as a diagonal matrix of the form $\bar{\varepsilon}_b = \varepsilon_0 \varepsilon_{diel} \bar{\mathbf{1}}$. In addition, it is assumed that the response of bound electrons is little affected by the static electric bias. Furthermore, we also neglect the chiral response inherent to materials with D_3 symmetry, which is associated with natural optical activity. Under these conditions, the permittivity takes the form $\bar{\varepsilon}(\omega) = \varepsilon_0 [\varepsilon_{diel} \bar{\mathbf{1}} + \bar{\chi}_D(\omega) + \bar{\chi}_{EO}^H(\omega) + \bar{\chi}_{EO}^{NH}(\omega)]$, where the electric susceptibilities $\bar{\chi}_\alpha(\omega) = i\bar{\sigma}_\alpha/(\varepsilon_0 \omega)$ model the different components of the free electrons response ($\alpha = $ D, EO$-$H, EO$-$NH). Doing this, the relative permittivity tensor of the material can be written as

$$\frac{\bar{\varepsilon}(\omega)}{\varepsilon_0} = \varepsilon_{diag} \bar{\mathbf{1}} + i\varepsilon_g \hat{\mathbf{z}} \times \bar{\mathbf{1}}, \quad \text{with} \tag{20a}$$

$$\varepsilon_{diag}(\omega) = \varepsilon_{diel} - \frac{\omega_p^2}{\omega^2 + i\Gamma\omega} \quad \text{and}$$

$$\varepsilon_g(\omega) = \frac{\omega_0 \Gamma}{\omega} \left(\frac{2}{\Gamma} + \frac{i\omega + \Gamma}{\omega^2 + \Gamma^2} \right). \tag{20b}$$

For the sake of simplicity, we will omit the dispersion of ε_{diel}, but we will incorporate dissipation effects due to phonon coupling, represented by a constant imaginary component: $\varepsilon_{diel} = \varepsilon'_{diel} + i\varepsilon''_{diel}$.

Next, we characterize the plane-wave modes in the material for propagation along the trigonal axis. The dispersion equation for this case can be simplified to $k_z^2 - (\omega/c)^2 (\varepsilon_{diag} \pm \varepsilon_g) = 0$. Solving this dispersion equation yields the following solutions:

$$\begin{array}{llll} \text{Eigenmode 1:} & k_{z,1} = \frac{\omega}{c}\sqrt{\varepsilon_{eff,1}} & \text{with} & \varepsilon_{eff,1} = \varepsilon_{diag} + \varepsilon_g, \quad \mathbf{E}_1 \sim \hat{\mathbf{x}} + i\hat{\mathbf{y}}, \\ \text{Eigenmode 2:} & k_{z,2} = \frac{\omega}{c}\sqrt{\varepsilon_{eff,2}} & \text{with} & \varepsilon_{eff,2} = \varepsilon_{diag} - \varepsilon_g, \quad \mathbf{E}_2 \sim \hat{\mathbf{x}} - i\hat{\mathbf{y}}. \end{array} \tag{21}$$

Therefore, the bulk material supports two eigenmodes: eigenmode 1 with positive handedness with respect to the $+z$ axis and eigenmode 2 with negative handedness with respect to $+z$.

Figure 2 shows the photonic band diagrams ($\omega = \omega' + i\omega''$ vs k_z) for different values of ω_0. In the absence of bias ($\omega_0 = 0$), the material supports the propagation of two degenerate modes [see blue lines in Figs. 2(a) and 2(b)]. Differently, under a static electric bias ($\omega_0 \neq 0$), two circularly polarized eigenmodes with opposite handedness propagate in the mate-

rial [see orange and green solid and dashed lines in Figs. 2(a) and 2(b)]. Notably, for eigenmode 2 (dashed lines) an increase of ω_0 diminishes $|\omega''|$—corresponding to a larger lifetime of the natural mode—and may even lead to oscillations that grow exponentially with time ($\omega'' > 0$) [see Fig. 2(b)]. These exponentially growing oscillations (wave instabilities) arise from the non-Hermitian electro-optic effect, which becomes significant for large enough values of $|\omega_0|$. Quite differently, for eigenmode 1 (solid lines) $|\omega''|$ increases with ω_0, so that the lifetime becomes shorter.
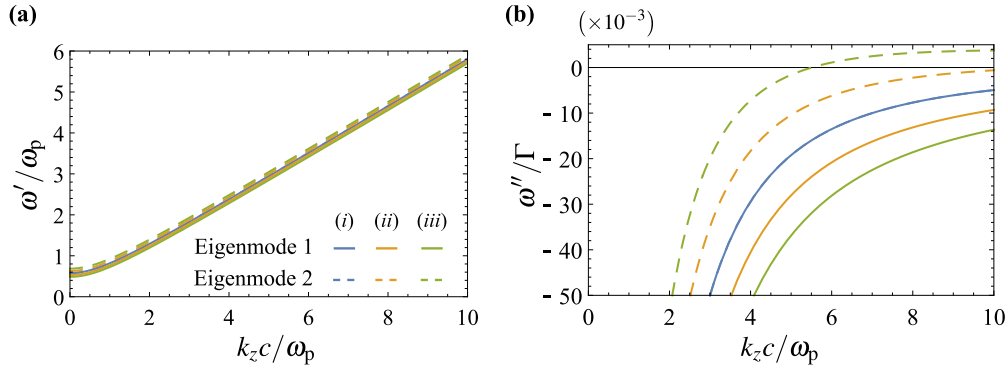
FIG. 2. Photonic band diagram of a conductive material with D_3 symmetry biased along the trigonal axis (z direction). The propagation is along z. (a) Real and (b) imaginary parts of the oscillation frequencies of the two eigenmodes as a function of k_z for $\varepsilon_{\mathrm{diel}} = 3$, $\omega_{\mathrm{p}}/(2\pi) = 5$ THz, $\Gamma = 0.03\omega_{\mathrm{p}}$, and (i) $\omega_0/\omega_{\mathrm{p}} = 0$, (ii) $\omega_0/\omega_{\mathrm{p}} = 0.15$, and (iii) $\omega_0/\omega_{\mathrm{p}} = 0.3$. For $\omega_0/\omega_{\mathrm{p}} = 0$, the solid and dashed blue curves are coincident in both panels.

As expected, accounting for losses in the dielectric response ($\varepsilon''_{\mathrm{diel}} \neq 0$) diminishes or even suppresses the gain (see Fig. 3). Finally, it should be noted that by reversing the sign of ω_0, which according to Eq. (16) implies a reversal of the sign of either E_0 or D, the roles of the two eigenmode polarizations are interchanged.

C. Stability

Let us analyze the conditions to have a stable material response. The material is stable when the bulk modes with an arbitrary real-valued k_z are associated with eigenfrequencies in the lower-half frequency plane ($\omega'' < 0$). To study this point, first we find the frequency ω where the dispersion diagram [$\omega = \omega(k_z)$] crosses the real-frequency axis. As $k_z = (\omega/c)\sqrt{\varepsilon_{\mathrm{diag}} \pm \varepsilon_{\mathrm{g}}}$, it follows that the crossing occurs for a frequency ω such that $\mathrm{Im}\{\varepsilon_{\mathrm{diag}} \pm \varepsilon_{\mathrm{g}}\} = 0$. Solving this equation, it is found that ω is linked to the gain term (ω_0) as

$$|\omega_0| = \frac{1}{\omega\Gamma}\left[\varepsilon''_{\mathrm{diel}}\omega(\omega^2 + \Gamma^2) + \Gamma\omega_{\mathrm{p}}^2\right]. \quad (22)$$

In order that $\omega(k_z)$ crosses the real-frequency axis exactly at the point ω the gain must be as in the above formula. The minimum gain to have a crossing can be found by minimizing the above expression with respect to ω. The minimum occurs

at the frequency $\omega_{\mathrm{th}} = \left(\frac{\Gamma\omega_{\mathrm{p}}^2}{2\varepsilon''_{\mathrm{diel}}}\right)^{1/3}$. Thus, the gain threshold is given by

$$|\omega_{0,\mathrm{th}}| = \frac{1}{\omega_{\mathrm{th}}\Gamma}\left[\varepsilon''_{\mathrm{diel}}\omega_{\mathrm{th}}(\omega_{\mathrm{th}}^2 + \Gamma^2) + \Gamma\omega_{\mathrm{p}}^2\right]. \quad (23)$$

For $|\omega_0| < |\omega_{0,\mathrm{th}}|$ the material response is unconditionally stable. When the gain matches the threshold value, the band diagram reaches the real-frequency axis exactly at the point $\omega' = \omega_{\mathrm{th}}$. Note that for $\varepsilon''_{\mathrm{diel}} = 0$, $\omega_{\mathrm{th}} \to \infty$ and $|\omega_{0,\mathrm{th}}| = 0$, indicating no instability threshold. This means that for $\varepsilon''_{\mathrm{diel}} = 0$ and sufficiently large frequencies, the system can always become unstable, consistent with the results shown in Fig. 2(b).

Figure 4(a) shows the dependence of $|\omega_{0,\mathrm{th}}|$ on the scattering rate Γ and on the imaginary part of the dielectric response $\varepsilon''_{\mathrm{diel}}$. It is evident from Fig. 4(a) that reducing $\varepsilon''_{\mathrm{diel}}$ results in a decrease of $|\omega_{0,\mathrm{th}}|$, whereas decreasing Γ leads to an increase of $|\omega_{0,\mathrm{th}}|$. Note that $|\omega_{0,\mathrm{th}}| \sim 1/\Gamma^{1/3}$, and hence, for $\Gamma = 0$, $|\omega_{0,\mathrm{th}}| \to \infty$.

Figure 4(b) shows how the threshold oscillation frequency ω_{th} (i.e., the instability frequency when the gain parameter matches the threshold) varies with Γ and $\varepsilon''_{\mathrm{diel}}$. For $\varepsilon''_{\mathrm{diel}} < \Gamma/(2\omega_{\mathrm{p}})$ the instability frequency is larger than ω_{p} [purple region in Fig. 4(b)], whereas for $\varepsilon''_{\mathrm{diel}} > \Gamma/(2\omega_{\mathrm{p}})$ it is smaller than ω_{p} [green region in Fig. 4(b)].
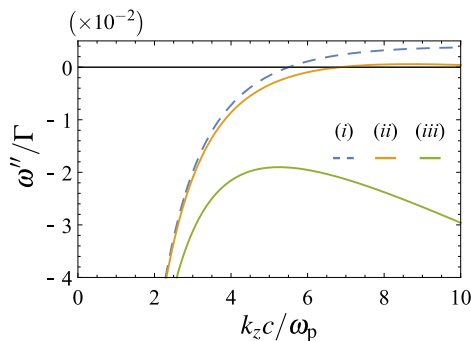

FIG. 3. Imaginary parts of the oscillation frequency of eigenmode 2 as a function of k_z for $\varepsilon_{\mathrm{diel}} = 3$, $\omega_0/\omega_{\mathrm{p}} = 0.3$, and $\Gamma = 0.03\omega_{\mathrm{p}}$. (i) $\varepsilon''_{\mathrm{diel}} = 0$; (ii) $\varepsilon''_{\mathrm{diel}} = 1 \times 10^{-4}$; (iii) $\varepsilon''_{\mathrm{diel}} = 1 \times 10^{-3}$.
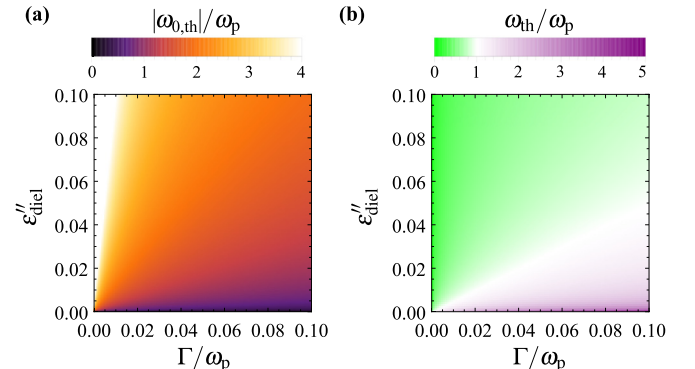
FIG. 4. (a) $|\omega_{0,\mathrm{th}}|$ and (b) ω_{th} as a function of the scattering rate Γ and of the imaginary part of the dielectric response $\varepsilon''_{\mathrm{diel}}$.
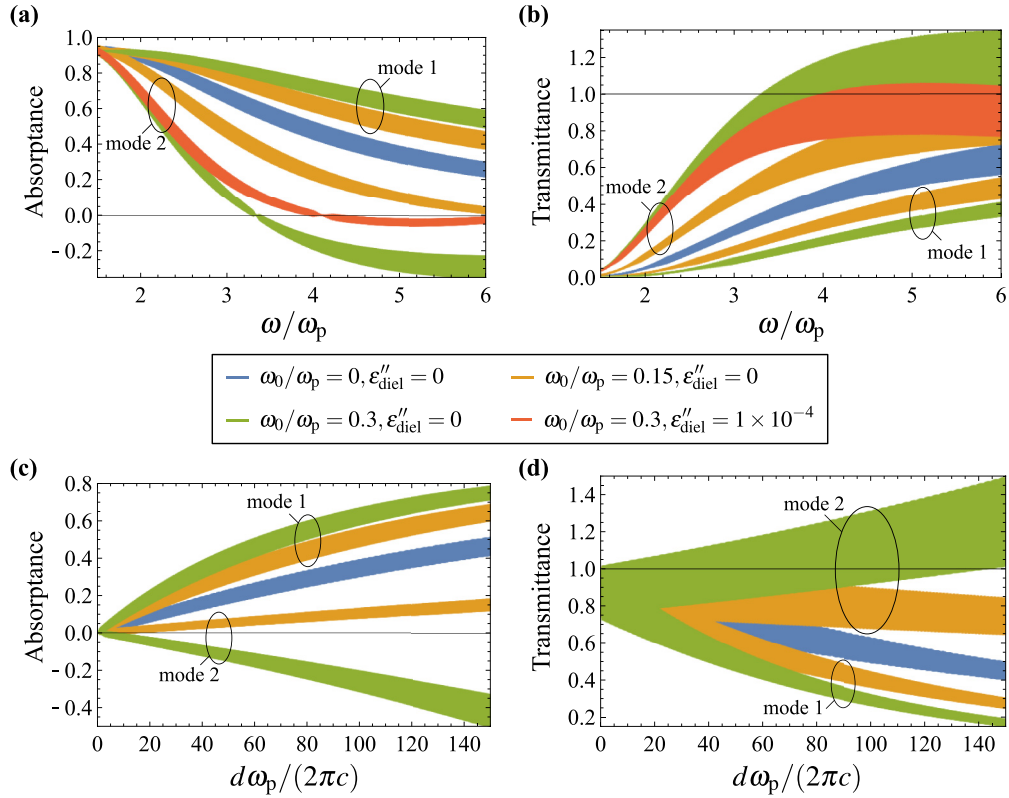
FIG. 5. (a) Absorptance and (b) transmittance as a function of the normalized frequency for an incident wave polarized as either mode 1 or mode 2. The normalized thickness of the material slab is $d\omega_p/(2\pi c) = 100$. (c) Absorptance and (d) transmittance as a function of the normalized thickness of the material slab for an incident wave polarized as either mode 1 or mode 2. The normalized frequency is $\omega/\omega_p = 5$. In all the panels, the material slab is characterized by $\varepsilon'_{\rm diel} = 3$, $\omega_p/(2\pi) = 5$ THz, and $\Gamma = 0.03\omega_p$. For $\omega_0/\omega_p = 0$ (blue curves) the absorptance and transmittance are polarization independent.

D. Transmission and absorption spectra

To study the impact of the non-Hermitian EO effect on the optical response of the 3D material, next we consider that a slab of thickness d is illuminated by a circularly polarized electromagnetic wave. We assume that the material slab interfaces are perpendicular to the trigonal axis (z direction). As before, the static electric bias ($\mathbf{E}_0$) is applied along the z direction, and the wave propagates along the direction of the bias (normal incidence). The material is surrounded by a vacuum.

For normal incidence, the gyrotropic material behaves as a standard dielectric with permittivity $\varepsilon_{\rm eff,1}$ ($\varepsilon_{\rm eff,2}$) for an incident electric field polarized as $\mathbf{E}_1 \sim \hat{\mathbf{x}} + i\hat{\mathbf{y}}$ ($\mathbf{E}_2 \sim \hat{\mathbf{x}} - i\hat{\mathbf{y}}$) [Eq. (21)]. Thus, the reflection and transmission coefficients take the form [57]

$$R = \frac{i(\eta_0^2 - \eta^2)\sin(\beta d)}{2\eta_0\eta\cos(\beta d) - i(\eta_0^2 + \eta^2)\sin(\beta d)}, \quad (24a)$$

$$T = \frac{2\eta_0\eta}{2\eta_0\eta\cos(\beta d) - i(\eta_0^2 + \eta^2)\sin(\beta d)}, \quad (24b)$$

where $\eta = \eta_0\sqrt{1/\varepsilon_{\rm eff}}$ and $\beta \equiv k_z = \frac{\omega}{c}\sqrt{\varepsilon_{\rm eff}}$ are the intrinsic impedance and propagation constant of the equivalent medium ($\varepsilon_{\rm eff,1}$ or $\varepsilon_{\rm eff,2}$), and η_0 is the intrinsic impedance of the vacuum. The reflectance $\mathcal{R}$ and transmittance $\mathcal{T}$ can be written in terms of the reflection and transmission coefficients

as $\mathcal{R} = |R|^2$ and $\mathcal{T} = |T|^2$. Finally, the absorptance $\mathcal{A}$ can be calculated from $\mathcal{A} = 1 - \mathcal{R} - \mathcal{T}$.

For an incoming wave that propagates along the $+z$ direction, an incident field of the type $\mathbf{E}_1 \sim \hat{\mathbf{x}} + i\hat{\mathbf{y}}$ corresponds to a right circularly polarized (RCP) wave, whereas an incident field of the type $\mathbf{E}_2 \sim \hat{\mathbf{x}} - i\hat{\mathbf{y}}$ corresponds to a left circularly polarized (LCP) wave. Conversely, when the incoming wave propagates along the $-z$ direction, illuminating the opposite face of the material slab, the mode $\mathbf{E}_1 \sim \hat{\mathbf{x}} + i\hat{\mathbf{y}}$ is associated with an LCP wave and the mode $\mathbf{E}_2 \sim \hat{\mathbf{x}} - i\hat{\mathbf{y}}$ is associated with a RCP wave. Thus, the transmittance for an RCP wave is $\mathcal{T} = \mathcal{T}_1$ when the direction of the incoming wave is $+z$, and $\mathcal{T} = \mathcal{T}_2$ when the direction of the incoming is $-z$. When the transmittances of modes 1 and 2 are different ($\mathcal{T}_1 \neq \mathcal{T}_2$) the system exhibits nonreciprocity [58].

In Fig. 5, we depict the absorption and transmission characteristics of the material, presenting their frequency dependence in panels (a) and (b), and their sensitivity to the variation of the material thickness in panels (c) and (d). The curves across all panels of Fig. 5 exhibit prominent Fabry-Perot oscillations, where the absorption and transmission peaks of the unbiased system (blue curves) are determined by $(\omega/c)\sqrt{\varepsilon'_{\rm diel}}d = n\pi$. Due to the very close proximity between adjacent Fabry-Perot resonances within the plotted scales, the curves exhibit a multitude of tightly packed oscillations. This creates a visual perception of curves with large thickness

dictated by the minima and maxima of the oscillations. The thickness of the curves is primarily influenced by the dielectric permittivity contrast between the material and the surrounding air region.

Figure 5(a) shows the absorptance of the electrically biased 3D slab as a function of frequency, for different values of ω_0/ω_p and $\varepsilon''_{\text{diel}}$, and for a normalized thickness $d\omega_p/(2\pi c) = 100$. When $\omega_0/\omega_p = 0$ (i.e., for an unbiased material or for a material without electro-optic response), the absorptances $\mathcal{A}_1$ and $\mathcal{A}_2$ of modes 1 and 2 are identical due to the rotational symmetry of the permittivity tensor [see Eq. (20)]. When $\omega_0/\omega_p \neq 0$, the material EO response combined with the intrinsic material loss induce circular dichroism, resulting in unequal absorptance for incident waves with opposite handedness ($\mathcal{A}_1 \neq \mathcal{A}_2$). Crucially, for sufficiently large values of ω_0/ω_p, the absorptance for incident waves polarized as $\mathbf{E}_2$ diminishes and may even become negative ($\mathcal{A}_2 < 0$) [see Fig. 5(a)], indicating the emergence of optical gain. In contrast, the absorptance for waves with the $\mathbf{E}_1$ polarization rises as ω_0/ω_p increases. The polarization-dependent optical gain is rooted in the non-Hermitian EO effect, the strength of which becomes significant for large enough ω_0/ω_p.

Remarkably, for large values of ω_0/ω_p the non-Hermitian EO response of the material may also lead to gain in transmission for waves with the $\mathbf{E}_2$ polarization. This is shown in Fig. 5(b), where the transmittance $\mathcal{T}_2$ can surpass unity for high enough ω_0/ω_p. Conversely, the transmittance for waves with the $\mathbf{E}_1$ polarization decreases as ω_0/ω_p increases, and never exceeds unity.

As expected, an increase in the value of the dielectric losses ($\varepsilon''_{\text{diel}}$) leads to a decrease in the gain, both in terms of absorption and transmission, potentially leading to its suppression [see the red curves in Figs. 5(a) and 5(b)].

Figures 5(c) and 5(d) depict the absorptance and transmittance of the electrically biased 3D material as a function of the slab thickness d, for different values of ω_0/ω_p and a fixed frequency of operation $\omega = 5\omega_p$. It is evident from Fig. 5(c) that increasing the slab thickness leads to a larger $|\mathcal{A}|$ (dissipation if $\mathcal{A} > 0$ or gain if $\mathcal{A} < 0$) for both polarization handednesses. Moreover, an increase in slab thickness results in higher (lower) transmittance values for mode 2 (mode 1) [see Fig. 5(d)].

IV. NON-HERMITIAN LINEAR ELECTRO-OPTIC EFFECT IN TELLURIUM

A. Optical response with DFT calculations

Tellurium (Te) is a promising material for the observation of the non-Hermitian linear EO effect. Under typical conditions, tellurium is a slightly p-doped chiral semiconductor with a gyrotropic noncentrosymmetric crystal structure [44]. However, it is noteworthy that under certain conditions, n-doping can also be achieved [59–63]. Interestingly, tellurium showcases the ability to exhibit large Berry curvature dipoles (D) near the Weyl points [44]. Various phenomena observed in tellurium, such as kinetic Faraday rotation [44–47], current-induced magnetization (kinetic magnetoelectric effect) [44,48,49], and the circular photogalvanic effect

[44,64–68], find their origin in the existence of the large Berry curvature dipoles.

Figures 6(a) and 6(b) illustrate the relation between the Berry curvature dipole (D) and the carrier density [hole density p in (a), and electron density n in (b)] as a function of the Fermi energy E_F. In addition, the dependence of the dc conductivities on E_F is shown in Figs. 6(c) and 6(d). The data is obtained from first-principles DFT calculations [44] (see the Appendix for the calculation methods). Notably, Fig. 6 reveals that n-doping of tellurium leads to larger magnitudes of the Berry curvature dipole compared to the more common p-doping scenario. Crucially, these large Berry curvature dipoles in n-doped tellurium emerge under conditions of low dc conductivities [see Fig. 6(d)]. Low conductivities are advantageous as they minimize Joule loss arising from the dc bias.

Elemental tellurium is a nonmagnetic semiconductor that forms two enantiomorphic trigonal structures with space groups P3$_1$21 (or D_3^4; right-handed structure) and P3$_2$21 (or D_3^6; left-handed structure), belonging to the 32 point group [44,69] discussed in Sec. III. Besides the screw symmetry along the trigonal z axis, the crystal structure also displays twofold rotational symmetry along three axes perpendicular to z. It is noteworthy that this screw symmetry along the trigonal z axis is directly linked to the helical-type current orbits discussed in Sec. II.

The Berry curvature dipole tensor of tellurium is equivalent to that given in Eq. (14) [44]. However, due to the anisotropy of the material, its electromagnetic behavior cannot be described by the relative permittivity tensor (20). Instead, tellurium is characterized by the following relative permittivity tensor:

$$\frac{\bar{\bar{\varepsilon}}(\omega)}{\varepsilon_0} = \varepsilon_\perp \bar{\mathbf{1}}_t + i\varepsilon_g \hat{\mathbf{z}} \times \bar{\mathbf{1}}_t + \varepsilon_\parallel \hat{\mathbf{z}} \otimes \hat{\mathbf{z}}, \tag{25}$$

with $\quad \bar{\mathbf{1}}_t = \bar{\mathbf{1}} - \hat{\mathbf{z}} \otimes \hat{\mathbf{z}}, \quad \varepsilon_\perp(\omega) = \varepsilon_{\text{diel},\perp} - \frac{\omega_{p,\perp}^2}{\omega^2 + i\Gamma\omega}, \quad \varepsilon_\parallel(\omega) = \varepsilon_{\text{diel},\parallel} - \frac{\omega_{p,\parallel}^2}{\omega^2 + i\Gamma\omega}$, and $\varepsilon_{\text{diel},l} = \varepsilon'_{\text{diel},l} + i\varepsilon''_{\text{diel},l}$ (with $l = \perp, \parallel$ denoting the directions perpendicular and parallel to the trigonal axis, respectively). As in Sec. III, for a static electric bias along the trigonal z axis, $\varepsilon_g(\omega) = \frac{\omega_0\Gamma}{\omega}\left(\frac{2}{\Gamma} + \frac{i\omega + \Gamma}{\omega^2 + \Gamma^2}\right)$. For simplicity, in Eq. (25) we neglect the chiral response of tellurium, which is responsible for its natural optical activity [46,70]. In what follows, relying on Eq. (25), as well as on first-principles calculations that provide the Berry curvature dipole D and the dc conductivity [44], we investigate several optical effects that arise from the gyrotropic and non-Hermitian linear EO responses of tellurium. For propagation along the z direction, the equivalent permittivities for modes 1 and 2 are now $\varepsilon_{\text{eff},1} = \varepsilon_\perp + \varepsilon_g$ and $\varepsilon_{\text{eff},2} = \varepsilon_\perp - \varepsilon_g$.

B. Kinetic Faraday effect, dichroism, and optical gain

To begin with, we investigate the rotation of light polarization in electrically biased tellurium. This current-induced Faraday effect was experimentally observed for the first time in Ref. [45] at a temperature of 77 K, and subsequently, new measurements were reported in Ref. [46]. We consider a system formed by a block of tellurium biased by a static
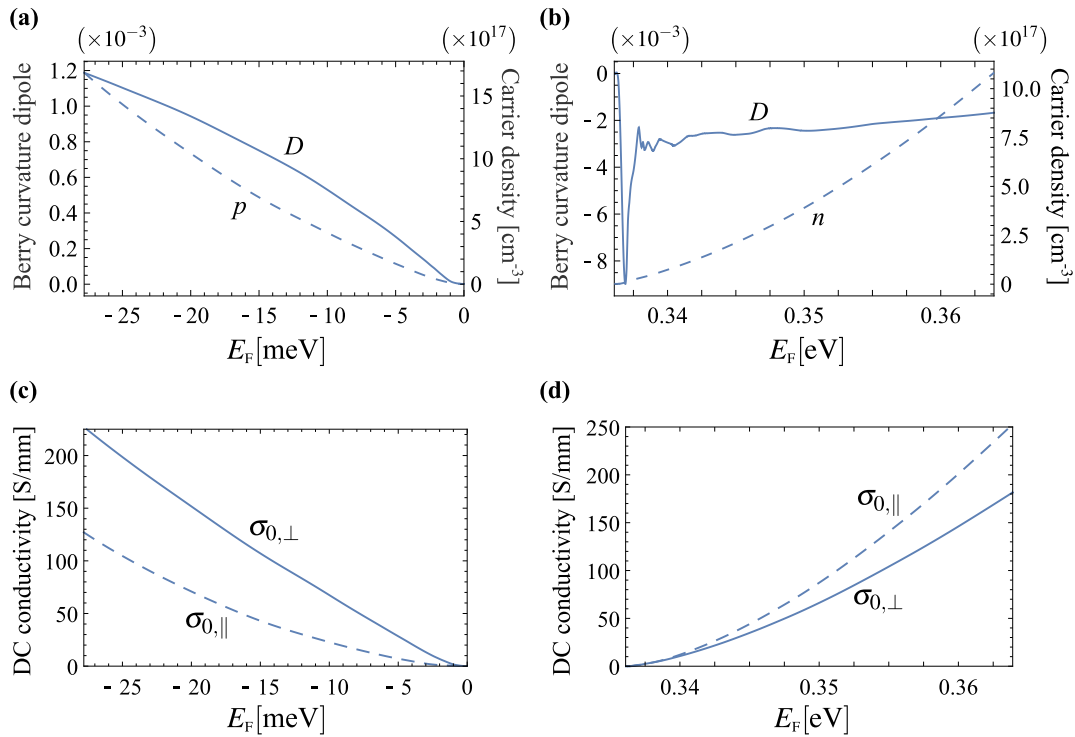
FIG. 6. (a) and (b) Berry curvature dipole D and carrier density (p or n) as a function of the Fermi energy E_F (measured from the top of the upper valence band) for (a) p-doped Te and (b) n-doped Te. (c) and (d) dc conductivities as a function of the Fermi energy E_F (assuming a scattering relaxation time $\tau = 0.64\,\mathrm{ps}$ [46]) for (c) p-doped Te and (d) n-doped Te.

electric field oriented along the z direction (trigonal axis) in between two linear polarizers [see Fig. 7(a)]. The linear polarizers consist of wire grids designed to fully absorb the electric field component parallel to the wires and allow the full transmission of the orthogonal component. The wires orientation of the input wire grid polarizer (WPG) is fixed along the x direction. As a result, for an incident wave propagating from the right to the left ($+z$ direction), the input WGP ensures that the field that illuminates the tellurium slab is oriented along the y direction. On the other hand, the output WGP is free to rotate in the xoy plane. The angle α defines the orientation of the wires of the output WGP [see Fig. 7(a)]. The output WPG fully suppresses the electric field component parallel to the wire axis direction defined by $\hat{\mathbf{u}}_\alpha = \cos(\alpha)\hat{\mathbf{x}} + \sin(\alpha)\hat{\mathbf{y}}$, while allowing the orthogonal component to pass through unchanged. We assume an operational frequency $f = 28.3\,\mathrm{THz}$ and a scattering relaxation time $\tau = 0.64\,\mathrm{ps}$, consistent with the parameters used in Ref. [46]. Additionally, the thickness of the Te block is $d = 12.5\,\mathrm{mm}$, as in Ref. [46]. Moreover, we estimate that for $f = 28.3\,\mathrm{THz}$ the dielectric response $\varepsilon_{\mathrm{diel},\perp} = 21.9 + 6.4 \times 10^{-4}i$. The dielectric response was determined through extrapolation from the experimental data presented in Ref. [71], using a fit with a Lorentz dispersion equation.

Figure 7(b) depicts the light intensity at the output (after the polarizer) as a function of the angle α for (i) an unbiased p-doped Te block and (ii) a biased p-doped Te block with $E_0 = 35.57\,\mathrm{V/mm}$ (which corresponds to $|\omega_0/\omega_{\mathrm{p},\perp}| \approx 2.2 \times 10^{-3}$). The transmission and reflection coefficients for an incoming wave with linear polarization can be found from

Eqs. (24), by writing the incident wave as a superposition of two circularly polarized waves with opposite handedness.

Notably, our results (blue dashed line) and the experimental results of Ref. [46] (blue star symbols) for the unbiased Te slab exhibit a good agreement. Note that the experimental results of [46] already exclude the field polarization rotation arising from the natural optical activity in tellurium. The E_0 values for these experimental results are estimated from the data available in Ref. [46] using $E_0 = j_z/(p\mu e)$, with j_z the electric current density along the z direction and μ the hole mobility. In this example the output light intensity $|\mathbf{E}^{\mathrm{out}}|^2$ for the biased system exhibits a slight decrease compared to the unbiased case. However, it is important to note that owing to the presence of Fabry-Perot resonances, the output intensity $|\mathbf{E}^{\mathrm{out}}|^2$ exhibits strong sensitivity to both the slab thickness d and the magnitude of the static electric field bias E_0. Even slight adjustments of d and/or E_0 can lead to a substantial change in the output amplitude. The system could be easily tuned to have an $|\mathbf{E}^{\mathrm{out}}|^2$ for the biased system larger (or smaller) than that for the unbiased system.

More interestingly, Fig. 7(b) shows that for $E_0 = 35.57\,\mathrm{V/mm}$ the polarization of an electromagnetic wave passing through the biased p-doped Te slab is rotated by $\pm 45°$. This suggests the potential for creating an optical isolator using an electrically biased (along the trigonal z axis) slab of p-doped Te. However, it is crucial to acknowledge that the required static electric bias magnitude is high (five times larger than the maximum E_0 employed in the experimental work [46]), probably rendering practical implementation unfeasible. One approach to circumvent this
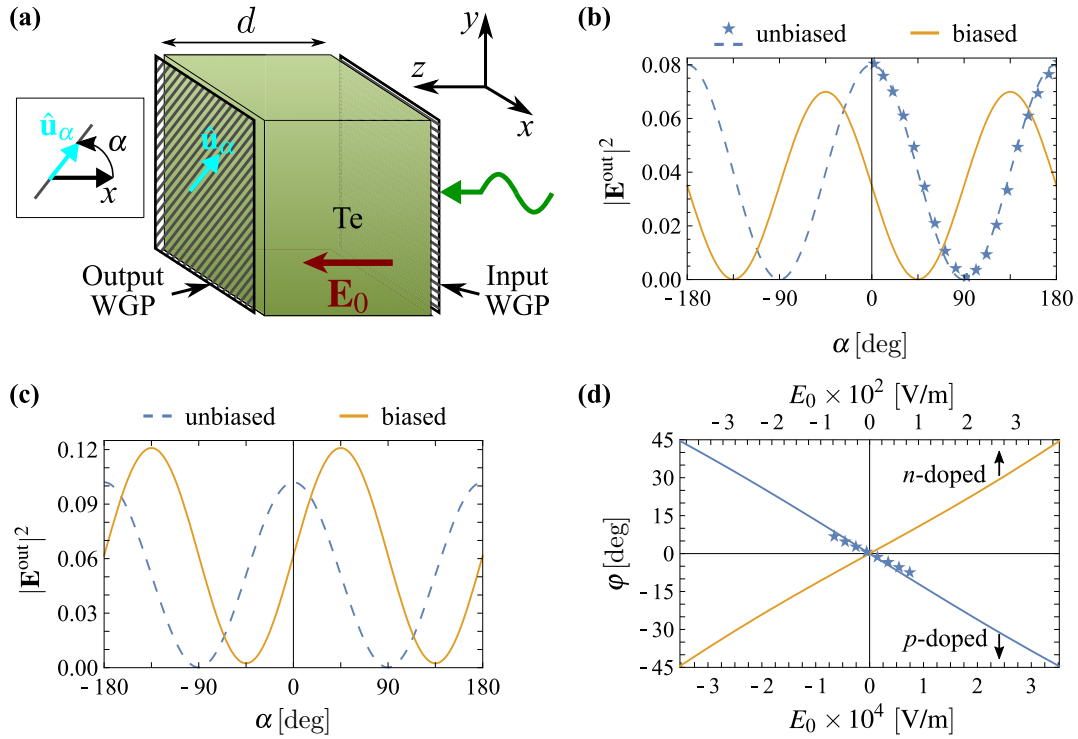
FIG. 7. (a) Electrically biased block of Te placed in between two linear polarizers. (b) and (c) Light intensity ($|\mathbf{E}^{\text{out}}|^2$) at the output (i.e., after the polarizer) as a function of orientation of the output WGP. (b) For p-doped Te with $p = 4 \times 10^{16}$ cm^{-3}, $D \approx 8.385 \times 10^{-5}$, and $\omega_{\text{p},\perp}/(2\pi) \approx 5.773$ THz, without a static electric bias (blue dashed line and star symbols), and with a bias $E_0 = 35.57$ V/mm. (c) For n-doped Te with $n = 0.784 \times 10^{16}$ cm^{-3}, $D \approx -8.99 \times 10^{-3}$, and $\omega_{\text{p},\perp}/(2\pi) \approx 1.857$ THz, without a static electric bias (blue dashed line), and with a bias, $E_0 = 0.39$ V/mm. (d) Electric field rotation ($\varphi = \alpha_1 - \alpha_0$) as a function of the static electric bias E_0. α_1 (α_0) corresponds to the angle α that provides maximum light intensity after the output WGP for a system biased with a static electric field E_0 (for an unbiased system); blue solid line and star symbols: p-doped Te slab with the same parameters as in panel (b); orange solid line: n-doped Te slab with the same parameters as in panel (c). In panels (b), (c), and (d) the frequency of operation is $f = 28.3$ THz, the thickness of the Te block is $d = 12.5$ mm, $\varepsilon_{\text{diel},\perp} = 21.9 + 6.4 \times 10^{-4}i$, and $\Gamma = 1.5625 \times 10^{12}$ rad/s. The blue star symbols in panels (b) and (d) correspond to the experimental results of Ref. [46].

problem is to use materials with much larger Berry curvature dipoles [72]. Another possibility involves using n-doped tellurium [59–63] instead of p-doped tellurium. Remarkably, n-doped tellurium can offer large values of the Berry curvature dipole D with low dc conductivity (see Fig. 6). Specifically, for p-doped tellurium and $p = 4 \times 10^{16}$ cm^{-3}, $D \approx 8.385 \times 10^{-5}$, $\sigma_{0,\perp} \approx 7.44$ S/mm, and $\sigma_{0,\parallel} \approx 1.1$ S/mm, whereas for n-doped tellurium and $n = 0.737 \times 10^{16}$ cm^{-3}, $D \approx -8.99 \times 10^{-3}$, $\sigma_{0,\perp} \approx 0.770$ S/mm, and $\sigma_{0,\parallel} \approx 1.229$ S/mm. However, it is important to note that for n-doped tellurium, when the optical frequency is non-negligible compared to the dominant interband transitions, the corrections to the semiclassical approximation used here can reduce the magnitude of D [44].

In Fig. 7(c), we show how the output light intensity $|\mathbf{E}^{\text{out}}|^2$ varies with the angle α for (i) an unbiased n-doped Te block and (ii) a biased n-doped Te block with $E_0 = 0.39$ V/mm (which corresponds to $|\omega_0/\omega_{\text{p},\perp}| \approx 0.808 \times 10^{-2}$). By comparing Figs. 7(b) and 7(c), it becomes evident that the relationship between the sign of the static field bias E_0 and the direction of the polarization rotation in a biased p-doped tellurium slab is opposite to that observed in a biased n-doped tellurium slab. This is a consequence of the differently signed Berry curvature dipoles: positive for p-doped tellurium and

negative for n-doped tellurium (see Fig. 6). More importantly, the results of Fig. 7(c) demonstrate that a 45° polarization rotation in the n-doped Te slab can be achieved by applying a much lower electric bias (specifically, $E_0 = 0.39$ V/mm), almost two orders of magnitude smaller than that needed for the same polarization rotation in the p-doped Te slab. Quite interestingly, $E_0 = 0.39$ V/mm is almost 18 times smaller than the maximum value of $E_0 = 7$ V/mm employed in the experiments reported in Ref. [46]. Thus, n-doped tellurium emerges as an interesting candidate for the practical realization of electrically biased optical isolators.

The sharp difference in the required static electric bias (E_0) for achieving equivalent polarization rotation in n-doped and p-doped Te becomes even more evident in Fig. 7(d). The figure depicts the dependence of the angle of rotation φ of the plane of polarization of $\mathbf{E}^{\text{out}}$ on the static electric bias E_0 for both p-doped and n-doped Te slabs. Notably, our theoretical results (blue solid line) and the experimental data from Ref. [46] (blue star symbols) for the p-doped Te slab concur very closely. Furthermore, as seen in Fig. 7(d), p-doped and n-doped Te slabs exhibit polarization rotations in opposite directions, in agreement with the results of Figs. 7(b) and 7(c). Finally, Fig. 7(d) shows that an n-doped Te slab requires
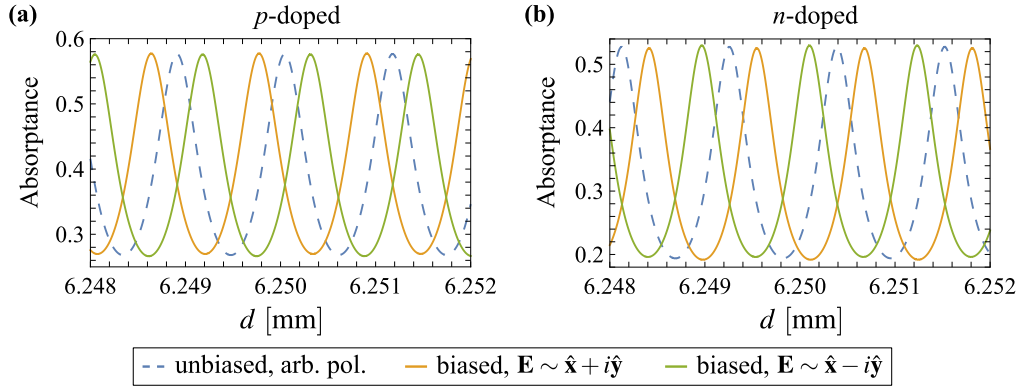
FIG. 8. Absorptance as a function of the thickness of the Te slab for a (a) p-doped and (b) n-doped material. Dashed blue lines: unbiased ($E_0 = 0$) Te for arbitrarily polarized incident waves; solid orange lines: biased Te for an incident wave polarized as mode 1 ($\mathbf{E}_1 \sim \hat{\mathbf{x}} + i\hat{\mathbf{y}}$); solid green lines: biased Te for an incident wave polarized as mode 2 ($\mathbf{E}_2 \sim \hat{\mathbf{x}} - i\hat{\mathbf{y}}$). (a) $p = 4 \times 10^{16}$ cm^{-3} and $E_0 = 75$ V/mm (which corresponds to $|\omega_0/\omega_{p,\perp}| \approx 4.638 \times 10^{-3}$); (b) $n = 0.784 \times 10^{16}$ cm^{-3} and $E_0 = 0.75$ V/mm (which corresponds to $|\omega_0/\omega_{p,\perp}| \approx 1.546 \times 10^{-2}$). The frequency of operation is $f = 28.3$ THz, $\varepsilon_{\text{diel},\perp} = 21.9 + 6.4 \times 10^{-4}i$, and $\Gamma = 1.5625 \times 10^{12}$ rad/s.

electric bias magnitudes ($|E_0|$) almost 100 times smaller than those needed by the p-doped Te to provide the same rotation of polarization φ.

Next, we investigate optical dichroism in an electrically biased tellurium slab. As before, we suppose that the tellurium slab is subjected to a static electric bias ($\mathbf{E}_0$) along the z direction (trigonal axis) and is illuminated by circularly polarized light propagating in the same z direction.

In Fig. 8, we present the absorptance characteristics of unbiased (dashed curves) and electrically biased (solid curves) p-doped [Fig. 8(a)] and n-doped [Fig. 8(b)] tellurium slabs as a function of slab thickness d and for a fixed frequency $f = 28.3$ THz. It is evident from Figs. 8(a) and 8(b) that the absorptance curves display a Fabry-Perot oscillation pattern. The absorption peaks of the unbiased system (dashed curves) are determined by $(\omega/c)\sqrt{\varepsilon'_{\text{diel},\perp}}d = n\pi$, where n is an integer.

For an unbiased system ($E_0 = 0$) and propagation along the z direction, the permittivity of tellurium is isotropic, leading to polarization-independent absorptance [see the blue dashed curves in Figs. 8(a) and 8(b); as before, we ignore the natural optical activity]. Notably, under a static electric bias ($E_0 \neq 0$), the absorptance becomes polarization dependent, and the absorptance peaks undergo a relative shift with respect to the unbiased case. The absorptance peaks associated with $\mathbf{E}_1 \sim \hat{\mathbf{x}} + i\hat{\mathbf{y}}$ and $\mathbf{E}_2 \sim \hat{\mathbf{x}} - i\hat{\mathbf{y}}$ polarized incident waves undergo opposite shifts, with one polarization shifted rightward and the other shifted leftward. Therefore, electrically biased tellurium exhibits optical dichroism. This optical dichroism arises from the combination of the gyrotropic Hermitian EO response with the intrinsic loss of Te and can become significant when E_0 (or $\omega_0/\omega_{p,\perp}$) reaches sufficiently high magnitudes. Within the parameter range considered in Figs. 8(a) and 8(b), the absorptances for modes 1 ($\mathcal{A}_1$) and 2 ($\mathcal{A}_2$) can differ by more than 54%. The results of Figs. 8(a) and 8(b) demonstrate that to achieve a comparable level of optical dichroism, the required magnitude of E_0 in the n-doped tellurium is two orders of magnitude lower than that needed in the p-doped tellurium. Notably, the magnitude of E_0 considered for the

n-doped tellurium ($E_0 = 0.75$ V/mm) is almost one order of magnitude below the maximum E_0 used in the experiments of Ref. [46] (specifically, $E_0 = 7$ V/mm). Furthermore, it is important to highlight that the value of E_0 can be further reduced by increasing the thickness of the tellurium block.

To conclude this section, we demonstrate that due to the non-Hermitian linear EO effect, tellurium may also provide optical gain. Figures 9(a) and 9(b) display how absorptance varies with the magnitude of the static electric bias (E_0) for both p-doped [Fig. 9(a)] and n-doped [Fig. 9(b)] tellurium. Quite remarkably, Figs. 9(a) and 9(b) show that when E_0 surpasses a certain threshold, the absorptance for circularly polarized incident waves of a certain handedness can become negative [see the green curve in Fig. 9(a) and the orange curve in Fig. 9(b)], indicating the emergence of optical gain. This gain regime emerges due to the nonconservative (transistor-type) light-matter interactions associated with the Berry curvature dipoles, which create the opportunity to have optical gain controlled by the polarization handedness.

For p-doped tellurium, $E_0 > 0$, and propagation along the $+z$ direction, the gain regime, associated with negative absorption, occurs for LCP incident waves [see the green curve in Fig. 9(a)]. However, achieving this gain response in p-doped tellurium requires exceptionally high values of E_0, exceeding 9.07 V/μm. In contrast, for n-doped tellurium the optical gain emerges for RCP incident waves [see the orange curve in Fig. 9(b)]. Crucially, in the case of n-doped tellurium, the gain response is unlocked for much lower static electric bias E_0, specifically $E_0 > 57$ V/mm. It is worth noting that these E_0 thresholds are consistent with the values obtained using Eqs. (16) and (22). Therefore, the magnitude of E_0 required for achieving optical gain in n-doped tellurium is more than two orders of magnitude smaller than that needed in p-doped tellurium. Unfortunately, applying an E_0 of the order of 57 V/mm poses significant practical challenges. Such a value is eight times larger than the maximum value of E_0 employed in the experiments of Ref. [46]. In future work, we will study other more practical configurations, or more advantageous materials with larger Berry curvature dipoles [72].
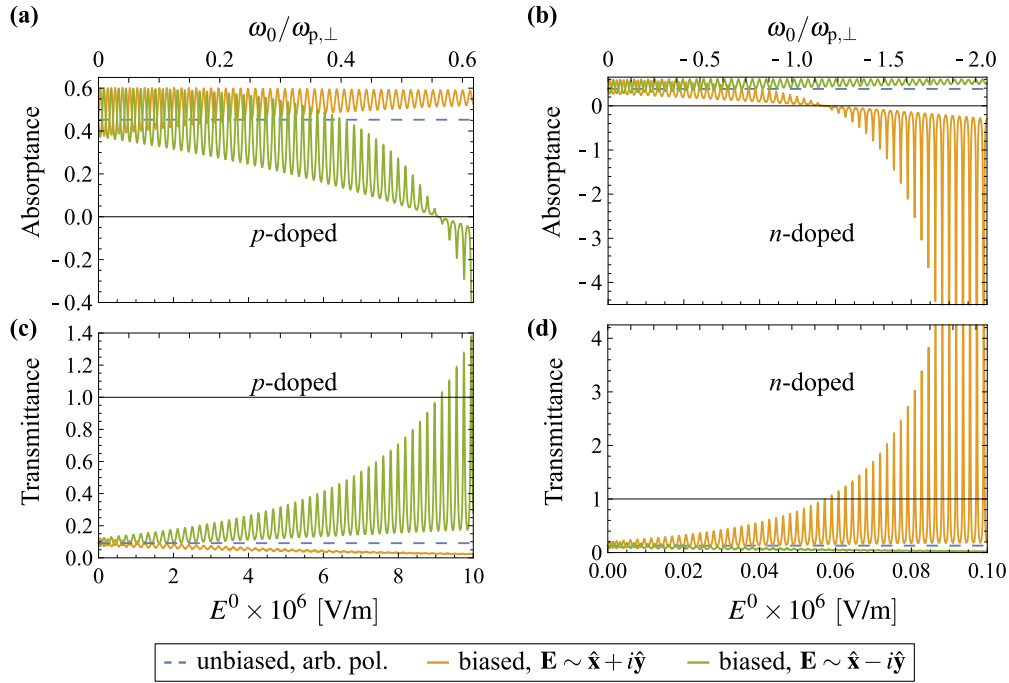
FIG. 9. (a),(b) Absorptance and (c),(d) transmittance as a function of the static electric field bias E_0 and $\omega_0/\omega_{p,\perp}$. (a),(c) *p*-doped Te with $p = 4 \times 10^{16}$ cm^{-3}; (b),(d) *n*-doped Te with $n = 0.784 \times 10^{16}$ cm^{-3}. Dashed blue lines: unbiased ($E_0 = 0$) Te for arbitrarily polarized incident waves; solid orange lines: biased Te for an incident wave polarized as mode 1 ($\mathbf{E}_1 \sim \hat{\mathbf{x}} + i\hat{\mathbf{y}}$); solid green lines: biased Te for an incident wave polarized as mode 2 ($\mathbf{E}_1 \sim \hat{\mathbf{x}} - i\hat{\mathbf{y}}$). The frequency of operation is $f = 28.3$ THz, the thickness of the Te slab is $d = 10$ mm, $\varepsilon_{\text{diel},\perp} = 21.9 + 6.4 \times 10^{-4}i$, and $\Gamma = 1.5625 \times 10^{12}$ rad/s.

In Figs. 9(c) and 9(d), we depict the transmittance as a function of the static electric bias magnitude (E_0) for both *p*-doped [Fig. 9(c)] and *n*-doped [Fig. 9(d)] tellurium. Notably, these results show that for large enough E_0, the *p*-doped (*n*-doped) tellurium may also provide transmission gain as the transmittance for LCP (RCP) incident waves may exceed unity. Analogous to the absorptance case, *n*-doped tellurium requires an E_0 roughly 100 times smaller to achieve the same transmission gain as with *p*-doped tellurium.

V. CONCLUSIONS

In this work, relying on first-principles DFT and Boltzmann transport theory, we have conducted a theoretical analysis of the linear EO effect within low-symmetry 3D conductive materials characterized by large Berry curvature dipoles. In line with Ref. [38], our study reveals the presence of two distinct contributions to the linear EO effect: one stemming from a gyrotropic Hermitian contribution linked to a conservative response, and another arising from a non-Hermitian electro-optic response characterized by its nonconservative nature. The gyrotropic Hermitian EO response may be pictured as being the result of helical-type microscopic currents induced by the static electric bias, leading to the generation of an internal static magnetic field. Remarkably, the Berry curvature dipole tensor may be understood as a magnetoelectric coupling tensor that relates the equivalent internal magnetic field to the static electric bias.

Our analysis was centered on 3D materials with D_3 symmetry under a static electric bias along the trigonal axis. It was demonstrated that such electrically biased materials

may potentially provide negative absorption (i.e., optical gain) and transmission amplification. Finally, we have identified trigonal tellurium as a promising material for exploring and leveraging the non-Hermitian EO effect. It was demonstrated that the gyrotropic Hermitian response of tellurium may enable realizing electrically biased electromagnetic isolators, as well as induce significant optical dichroism. Moreover, under extreme conditions of operation, the non-Hermitian electro-optic response of tellurium can lead to optical gain. In such scenarios, *n*-doped tellurium is especially noteworthy due to its larger Berry curvature dipoles and lower dc conductivity, as compared to the commonly used *p*-doped tellurium.

APPENDIX: DFT CALCULATION METHODS

Here, we provide a detailed description of the methodology used for the first-principles DFT calculations. Drawing from previous studies [44,73,74], our approach involved density functional band-structure calculations using the VASP code [75]. These calculations incorporated spin-orbit coupling and employed the HSE06 hybrid functional [76], utilizing a $6 \times 6 \times 8$ grid of k points. This way, we obtained an energy gap of 0.312 eV, which agrees well with both the calculated value of 0.314 eV from the GW method [77] and the experimental value of 0.323 eV [78]. In order to interpolate the bands and Berry curvature on an ultradense grid of k points, we construct Wannier functions, as implemented in

the WANNIER90 code [79] using the s and p orbitals of Te as initial projections (24 Wannier functions in total). More details on the DFT calculations and Wannierization can be found in [73].

The difference here is that we do not use the maximal localization technique [80], but just disentanglement and projections [81]. Furthermore, to avoid any artifacts arising from numerical inaccuracies causing the Wannier functions to break symmetries, we symmetrize the Wannier Hamiltonian and position matrix elements, following the procedure described in [82] and implemented in the WANNIERBERRI code [83]. To accurately evaluate the integral for the Berry curvature dipole, we note that only k points in the vicinity of the H point contribute significantly. Thus, we sample the irreducible wedge around the H point with a grid of points spaced by no less than 0.004 Å^{-1}, and then perform 400 adaptive refinement iterations [83] to ensure convergence. We use the "Fermi sea" formulation [right-hand side of Eq. (11)] with the Berry curvature gradient evaluated following [84] and Fermi factors evaluated with the tetrahedron method.

[1] F. Koenderink, A. Alù, and A. Polman, Nanophotonics: Shrinking light-based technology, Science **348**, 516 (2015).

[2] A. Karabchevsky, A. Katiyi, A. S. Ang, and A. Hazan, On-chip nanophotonics and future challenges, Nanophotonics **9**, 3733 (2020).

[3] Z. Zhou, B. Yin, and J. Michel, On-chip light sources for silicon photonics, Light Sci. Appl. **4**, e358 (2015).

[4] J. B. Khurgin, How to deal with the loss in plasmonics and metamaterials, Nat. Nanotechnol. **10**, 2 (2015).

[5] S. V. Boriskina, T. A. Cooper, L. Zeng, G. Ni, J. K. Tong, Y. Tsurimaki, Y. Huang, L. Meroueh, G. Mahan, and G. Chen, Losses in plasmonics: From mitigating energy dissipation to embracing loss-enabled functionalities, Adv. Opt. Photonics **9**, 775 (2017).

[6] M. Levy, The on-chip integration of magnetooptic waveguide isolators, IEEE J. Sel. Top. Quantum Electron. **8**, 1300 (2002).

[7] C. Caloz, A. Alù, S. Tretyakov, D. Sounas, K. Achouri, and Z.-L. Deck-Léger, Electromagnetic nonreciprocity, Phys. Rev. Appl. **10**, 047001 (2018).

[8] M. Freiser, A survey of magnetooptic effects, IEEE Trans. Magn. **4**, 152 (1968).

[9] J. D. Adam, L. E. Davis, G. F. Dionne, E. F. Schloemann, and S. N. Stiltzer, Ferrite devices and materials, IEEE Trans. Microwave Theory Technol. **50**, 721 (2002).

[10] H. Dötsch, N. Bahlmann, O. Zhuromskyy, M. Hammer, L. Wilkens, R. Gerhardt, P. Hertel, and A. F. Popkov, Applications of magneto-optical waveguides in integrated optics: Review, J. Opt. Soc. Am. B **22**, 240 (2005).

[11] Z. Yu and S. Fan, Complete optical isolation created by indirect interband photonic transitions, Nat. Photonics **3**, 91 (2009).

[12] D. L. Sounas, C. Caloz, and A. Alù, Giant non-reciprocity at the subwavelength scale using angular momentum-biased metamaterials, Nat. Commun. **4**, 2407 (2013).

[13] D. L. Sounas and A. Alu, Non-reciprocal photonics based on time modulation, Nat. Photonics **11**, 774 (2017).

[14] E. Galiffi, R. Tirole, S. Yin, H. Li, S. Vezzoli, P. A. Huidobro, M. G. Silveirinha, R. Sapienza, A. Alù, and J. B. Pendry, Photonics of time-varying media, Adv. Photonics **4**, 014002 (2022).

[15] R. Fleury, D. L. Sounas, C. F. Sieck, M. R. Haberman, and A. Alu, Sound isolation and giant linear nonreciprocity in a compact acoustic circulator, Science **343**, 516 (2014).

[16] S. Lannèbere and M. G. Silveirinha, Wave instabilities and unidirectional light flow in a cavity with rotating walls, Phys. Rev. A **94**, 033810 (2016).

[17] B. V. Duppen, A. Tomadin, A. N. Grigorenko, and M. Polini, Current-induced birefringent absorption and non-reciprocal plasmons in graphene, 2D Mater. **3**, 015011 (2016).

[18] T. A. Morgado and M. G. Silveirinha, Drift-induced unidirectional graphene plasmons, ACS Photonics **5**, 4253 (2018).

[19] T. A. Morgado and M. G. Silveirinha, Nonlocal effects and enhanced nonreciprocity in current-driven graphene systems, Phys. Rev. B **102**, 075102 (2020).

[20] T. A. Morgado and M. G. Silveirinha, Directional dependence of the plasmonic gain and nonreciprocity in drift-current biased graphene, Nanophotonics **11**, 4929 (2022).

[21] W. Zhao *et al.*, Efficient Fizeau drag from Dirac electrons in monolayer graphene, Nature (London) **594**, 517 (2021).

[22] Y. Dong *et al.*, Fizeau drag in graphene plasmonics, Nature (London) **594**, 513 (2021).

[23] T. Kodera, D. L. Sounas, and C. Caloz, Artificial Faraday rotation using a ring metamaterial structure without static magnetic field, Appl. Phys. Lett. **99**, 031114 (2011).

[24] Z. Wang, Z. Wang, J. Wang, B. Zhang, J. Huangfu, J. D. Joannopoulos, M. Soljačić, and L. Ran, Gyrotropic response in the absence of a bias field, Proc. Natl. Acad. Sci. USA **109**, 13194 (2012).

[25] T. Kodera, D. L. Sounas, and C. Caloz, Magnetless non-reciprocal metamaterial (MNM) technology: Application to microwave components, IEEE Trans. Microwave Theory Tech. **61**, 1030 (2013).

[26] S. Buddhiraju, A. Song, G. T. Papadakis, and S. Fan, Nonreciprocal metamaterial obeying time-reversal symmetry, Phys. Rev. Lett. **124**, 257403 (2020).

[27] M. Scalora, J. P. Dowling, C. M. Bowden, and M. J. Bloemer, The photonic band edge optical diode, J. Appl. Phys. **76**, 2023 (1994).

[28] M. D. Tocci, M. J. Bloemer, M. Scalora, J. P. Dowling, and C. M. Bowden, Thin-film nonlinear optical diode, Appl. Phys. Lett. **66**, 2324 (1995).

[29] K. Gallo and G. Assanto, All-optical diode based on second-harmonic generation in an asymmetric waveguide, J. Opt. Soc. Am. B **16**, 267 (1999).

[30] I. V. Shadrivov, V. A. Fedotov, D. A. Powell, Y. S. Kivshar, and N. I. Zheludev, Electromagnetic wave analogue of an electronic diode, New J. Phys. **13**, 033025 (2011).

[31] A. M. Mahmoud, A. R. Davoyan, and N. Engheta, All-passive nonreciprocal metastructure, Nat. Commun. **6**, 8359 (2015).

[32] D. L. Sounas, J. Soric, and A. Alu, Broadband passive isolators based on coupled nonlinear resonances, Nat. Electronics **1**, 113 (2018).

[33] Y. Shi, Z. Yu, and S. Fan, Limitations of nonlinear optical isolators due to dynamic reciprocity, Nat. Photonics **9**, 388 (2015).

[34] D. E. Fernandes and M. G. Silveirinha, Asymmetric transmission and isolation in nonlinear devices: Why they are different, IEEE Antennas Wirel. Propag. Lett. **17**, 1953 (2018).

[35] M. Suárez-Rodríguez *et al.*, Odd nonlinear conductivity under spatial inversion in chiral tellurium, Phys. Rev. Lett. **132**, 046303 (2024).

[36] I. Sodemann and L. Fu, Quantum nonlinear Hall effect induced by Berry curvature dipole in time-reversal invariant materials, Phys. Rev. Lett. **115**, 216806 (2015).

[37] P. Makushko *et al.*, A tunable room-temperature nonlinear Hall effect in elemental bismuth thin films, Nat. Electron. **7**, 207 (2024).

[38] T. G. Rappoport, T. A. Morgado, S. Lannebère, and M. G. Silveirinha, Engineering transistorlike optical gain in two-dimensional materials with Berry curvature dipoles, Phys. Rev. Lett. **130**, 076901 (2023).

[39] S. Lannebère, D. E. Fernandes, T. A. Morgado, and M. G. Silveirinha, Nonreciprocal and non-Hermitian material response inspired by semiconductor transistors, Phys. Rev. Lett. **128**, 013902 (2022).

[40] A. Hakimi, K. Rouhi, T. G. Rappoport, M. G. Silveirinha, and F. Capolino, Chiral terahertz lasing with Berry curvature dipoles, arXiv:2312.15142.

[41] D. Vanderbilt, Topological insulators and semimetals, *Berry Phases in Electronic Structure Theory: Electric Polarization, Orbital Magnetization and Topological Insulators* (Cambridge University Press, Cambridge, 2018), pp. 201–275.

[42] D. Xiao, M.-C. Chang, and Q. Niu, Berry phase effects on electronic properties, Rev. Mod. Phys. **82**, 1959 (2010).

[43] Y. Gao, S. A. Yang, and Q. Niu, Field induced positional shift of Bloch electrons and its dynamical implications, Phys. Rev. Lett. **112**, 166601 (2014).

[44] S. S. Tsirkin, P. A. Puente, and I. Souza, Gyrotropic effects in trigonal tellurium studied from first principles, Phys. Rev. B **97**, 035158 (2018).

[45] L. E. Vorob'ev, E. L. Ivchenko, G. E. Pikus, I. I. Farbshtein, V. A. Shalygin, and A. V. Shturbin, Optical activity in tellurium induced by a current, Pis'ma Zh. Eksp. Teor. Fiz. **29**, 485 (1979) [JETP Lett. **29**, 441 (1979)].

[46] V. A. Shalygin, A. N. Sofronov, L. E. Vorob'ev, and I. I. Farbshtein, Current-induced spin polarization of holes in tellurium, Phys. Solid State **54**, 2362 (2012).

[47] E. J. König, M. Dzero, A. Levchenko, and D. A. Pesin, Gyrotropic Hall effect in Berry-curved materials, Phys. Rev. B **99**, 155404 (2019).

[48] T. Furukawa, Y. Shimokawa, K. Kobayashi, and T. Itou, Observation of current-induced bulk magnetization in elemental tellurium, Nat. Commun. **8**, 954 (2017).

[49] T. Furukawa, Y. Watanabe, N. Ogasawara, K. Kobayashi, and T. Itou, Current-induced magnetization caused by crystal chirality in nonmagnetic elemental tellurium, Phys. Rev. Res. **3**, 023111 (2021).

[50] L.-K. Shi, O. Matsyshyn, J. C. W. Song, and I. S. Villadiego, Berry-dipole photovoltaic demon and the thermodynamics of photocurrent generation within the optical gap of metals, Phys. Rev. B **107**, 125151 (2023).

[51] J. Son, K.-H. Kim, Y. H. Ahn, H.-W. Lee, and J. Lee, Strain engineering of the Berry curvature dipole and valley magnetization in monolayer MoS$_2$, Phys. Rev. Lett. **123**, 036806 (2019).

[52] T. Yoda, T. Yokoyama, and S. Murakami, Current-induced orbital and spin magnetizations in crystals with helical structure, Sci. Rep. **5**, 12024 (2015).

[53] T. Yoda, T. Yokoyama, and S. Murakami, Orbital Edelstein effect as a condensed-matter analog of solenoids, Nano Lett. **18**, 916 (2018).

[54] D. Hara, M. S. Bahramy, and S. Murakami, Current-induced orbital magnetization in systems without inversion symmetry, Phys. Rev. B **102**, 184404 (2020).

[55] N. B. Baranova, Y. V. Bogdanov, and B. Y. Zel'Dovich, Electrical analog of the Faraday effect and other new optical effects in liquids, Opt. Commun. **22**, 243 (1977).

[56] Y. Onishi and L. Fu, High-efficiency energy harvesting based on nonlinear Hall rectifier, arXiv:2211.17219.

[57] D. M. Pozar, *Microwave Engineering* (Wiley, New York, 2006).

[58] F. R. Prudêncio and M. G. Silveirinha, Optical isolation of circularly polarized light with a spontaneous magnetoelectric effect, Phys. Rev. A **93**, 043846 (2016).

[59] R. N. Ghoshtagore, Self-diffusion in tellurium. I. Anisotropy and impurity effect, Phys. Rev. **155**, 598 (1967).

[60] Y. Nonoguchi, F. Kamikonya, K. Ashiba, K. Ohashi, and T. Kawai, Air-stable *n*-type tellurium nanowires coordinated by large organic salts, Synth. Met. **225**, 93 (2017).

[61] G. Qiu, M. Si, Y. Wang, X. Lyu, W. Wu, and P. Ye, High-performance few-layer tellurium CMOS devices enabled by atomic layer deposited dielectric doping technique, in *Proceedings of the 2018 76th Device Research Conference (DRC)* (IEEE, New York, 2018).

[62] G. Qiu, C. Niu, Y. Wang, M. Si, Z. Zhang, W. Wu, and P. D. Ye, Quantum Hall effect of Weyl fermions in *n*-type semiconducting tellurene, Nat. Nanotechnol. **15**, 585 (2020).

[63] C. Niu, G. Qiu, Y. Wang, M. Si, W. Wu, and P. D. Ye, Bilayer quantum Hall states in an n-type wide tellurium quantum well, Nano Lett. **21**, 7527 (2021).

[64] E. L. Ivchenko and G. E. Pikus, New photogalvanic effect in gyrotropic crystals, Pis'ma Zh. Eksp. Teor. Fiz. **27**, 640 (1978) [JETP Lett. **27**, 604 (1978)].

[65] V. I. Belinicher, Space-oscillating photocurrent in crystals without symmetry center, Phys. Lett. A **66**, 213 (1978).

[66] V. M. Asnin, A. A. Bakun, A. M. Danishevskii, E. L. Ivchenko, G. E. Pikus, and A. A. Rogachev, Observation of a photo-emf that depends on the sign of the circular polarization of the light, Zh. Eksp. Teor. Fiz. Pisma Red. **28**, 80 (1978) [JETP Lett. **28**, 74 (1978)].

[67] V. M. Asnin, A. A. Bakun, A. M. Danishevskii, E. L. Ivchenko, G. E. Pikus, and A. A. Rogachev, "Circular" photogalvanic effect in optically active crystals, Solid State Commun. **30**, 565 (1979).

[68] L. E. Golub, E. L. Ivchenko, and B. Spivak, Semiclassical theory of the photogalvanic effect in noncentrosymmetric systems, Phys. Rev. B **102**, 085202 (2020).

[69] R. H. Asendorf, Space group of tellurium and selenium, J. Chem. Phys. **27**, 11 (1957).

[70] S. Fukuda, T. Shiosaki, and A. Kawabata, Infrared optical activity in tellurium, Phys. Status Solidi B **68**, K107 (1975).

[71] P. Grosse and W. Ritcher, Absorption spectra of tellurium in the spectral range from 18 to 460 cm^{-1}, Phys. Status Solidi B **41**, 239 (1970).

[72] Y. Zhang, Y. Sun, and B. Yan, Berry curvature dipole in Weyl semimetal materials: An *ab initio* study, Phys. Rev. B **97**, 041101(R) (2018).

[73] S. S. Tsirkin, I. Souza, and D. Vanderbilt, Composite Weyl nodes stabilized by screw symmetry with and without time-reversal invariance, Phys. Rev. B **96**, 045102 (2017).

[74] X. Liu, I. Souza, and S. S. Tsirkin, Electrical magnetochiral anisotropy in trigonal tellurium from first principles, arXiv:2303.10164.

[75] G. Kresse and J. Hafner, *Ab initio* molecular dynamics for open-shell transition metals, Phys. Rev. B **48**, 13115 (1993).

[76] A. V. Krukau, O. A. Vydrov, A. F. Izmaylov, and G. E. Scuseria, Influence of the exchange screening parameter on the performance of screened hybrid functionals, J. Chem. Phys. **125**, 224106 (2006).

[77] M. Hirayama, R. Okugawa, S. Ishibashi, S. Murakami, and T. Miyake, Weyl node and spin texture in trigonal tellurium and selenium, Phys. Rev. Lett. **114**, 206401 (2015).

[78] V. B. Anzin, M. I. Eremets, Y. V. Kosichkin, A. I. Nadezhdinskii, and A. M. Shirokov, Measurement of the energy gap in tellurium under pressure, Phys. Status Solidi A **42**, 385 (1977).

[79] G. Pizzi *et al.*, Wannier90 as a community code: New features and applications, J. Phys.: Condens. Matter **32**, 165902 (2020).

[80] N. Marzari and D. Vanderbilt, Maximally localized generalized Wannier functions for composite energy bands, Phys. Rev. B **56**, 12847 (1997).

[81] I. Souza, N. Marzari, and D. Vanderbilt, Maximally localized Wannier functions for entangled energy bands, Phys. Rev. B **65**, 035109 (2001).

[82] D. Gresch, Q. S. Wu, G. W. Winkler, R. Häuselmann, M. Troyer, and A. A. Soluyanov, Automated construction of symmetrized Wannier-like tight-binding models from *ab initio* calculations, Phys. Rev. Mater. **2**, 103805 (2018).

[83] S. S. Tsirkin, High performance Wannier interpolation of Berry curvature and related quantities with WannierBerri code, npj Comput. Mater. **7**, 33 (2021).

[84] X. Liu, I. Souza, and S. S. Tsirkin, Covariant derivatives of Berry-type quantities: Application to nonlinear transport, arXiv:2303.10129.